Intraseasonal Variability
in a Two-Layer Model and Observations

by

Christian L. Keppenne
NASA Goddard Space Flight Center
Greenbelt, Maryland 20771

Steven L. Marcus*
Jet Propulsion Laboratory
Pasadena, CA 91109

Masahide Kimoto
Center for Climate System Research
University of Tokyo
4-6-1 Komaba, Megoro-ku, Tokyo 153 Japan

Michael Ghil
Department of Atmospheric Sciences and
Institute of Geophysics and Planetary Physics
University of California, Los Angeles, CA 90095

Revised Version
May 1999

* Corresponding author

Abstract

A two-layer shallow-water model with R15 truncation and topographic forcing is used to study intraseasonal variability in the Northern Hemisphere's (NH) extratropical atmosphere. The model's variability is dominated by oscillations with average periods near 65–70 and 40–50 days. These periods are also found in 13.5 years of daily upper-air data from January 1980 to July 1993.

The spatial variability associated with these oscillations is examined by compositing the streamfunction-anomaly fields of the model and the observations. The model's 70-day oscillation is strongest in the Euro-Atlantic sector, where it bears a close resemblance to observed streamfunction composites of the North Atlantic Oscillation. The observed 70-day mode exhibits similar features in the Euro-Atlantic sector, accompanied by a north-south "seesaw" over the Pacific and Eurasia. Previous authors, in their analysis of geopotential height observations, also found these features to be present in an empirical orthogonal function that contains aspects of both the North Pacific and North Atlantic Oscillations.

The 40-day oscillation is characterized, in both the model simulations and observed data, by a zonal wavenumber-two pattern anchored over the NH topography. This pattern undergoes tilted-trough vacillation in both the model and observations. This midlatitude vacillation is strongest in the Pacific-North American sector, where it resembles a 40-day oscillation in the UCLA general circulation model that is largely driven by mountain torques over the Rockies. Comparisons with observational data show a clear separation between a tropical 50-day oscillation, not present in our model results, and a 40-day NH extratropical oscillation which resembles the topographically induced oscillation that arises in our two-layer model.

1

1 Introduction and motivation

Intraseasonal variability of large-scale atmospheric flow patterns has attracted considerable attention in recent years. The term is generally used to characterize phenomena associated with periods between 10 and 100 days. The corresponding frequency band contains more power than either the interannual or the synoptic band (Ghil and Mo 1991a; Kimoto and Ghil 1993a,b).

Interest for intraseasonal variability was stimulated by Madden and Julian's (1971, 1972) discovery of a 40–50-day oscillation in time series of tropical convection and zonal wind data. Oscillations in this frequency range have since been found in a variety of tropical data sets (e.g., Yasunari 1981; Lau and Chan 1985; Ghil and Mo 1991a). Another strong intraseasonal signal — this one active in the Northern Hemisphere (NH) extratropics — was identified separately in highly simplified (Legras and Ghil 1985; Jin and Ghil 1990) and in intermediate-resolution (Strong et al. 1993, 1995) barotropic models, as well as in a general circulation model (GCM — Marcus et al. 1994, 1996), and in observational data (Dickey et al., 1991; Ghil and Mo 1991a; Magaña, 1993). Weickmann et al. (1985) also suggested the existence of a 28–72 day signal in the NH extratropics, loosely synchronized with the tropical Madden-Julian oscillation (MJO).

The present paper's argument is that NH intraseasonal variability is dominated by oscillations with dynamic origins in the NH extratropics: a 40-day oscillation, which interacts with but is distinct from the tropical MJO, and a 70-day oscillation, which is linked to the intraseasonal variability of the North Atlantic Oscillation (Hurrell 1995). Higher-frequency intraseasonal signals with a period near 23–25 days were also identified in observational data by Branstator (1987), Kushnir (1987),

and Ghil and Mo (1991a,b). These two signals will be the subject of future investigation.

Our work continues a series of modeling and observational studies aimed at describing extratropical intraseasonal variability and identifying the mechanisms responsible for it. Legras and Ghil (1985; LG hereafter) detected a zonal-wavenumber two oscillation with a mean period of 36–40 days in a simplified equivalent-barotropic, quasi-geostrophic (QG) model with symmetry about the equator and idealized NH topography. Based on their preliminary results, Ghil (1987) hypothesized that this oscillation is due to an instability of nonzonal westerly flow caused by the jet stream's interaction with NH midlatitude mountain ranges. Jin and Ghil's (1990) weakly nonlinear analysis of a β-channel version of the LG model provided supporting evidence for this hypothesis by identifying a Hopf bifurcation that arises by the unstable, oscillatory interaction of the westerly jet with topography and yields a period lower than that associated with Rossby-wave dispersion. Tribbia and Ghil (1990) increased the resolution of LG's model, removed its artificial symmetries, and introduced a realistic topography. Their results also confirm the above hypothesis.

Marcus (1990) detected a 40-day oscillation in the NH extratropics of the global UCLA General Circulation Model (GCM) while using a version in which the MJO was essentially absent. Marcus et al. (1994, 1996) recognized instability of the jet stream over topography as the mechanism leading to this oscillation, which had been observed in NH data as well (Dickey et al. 1991; Ghil and Mo 1991a; Kimoto et al. 1991). Plaut and Vautard (1994 — henceforth PV94) found a 70-day oscillation, active during NH winter, while analyzing 700-mb height anomalies over the North Atlantic sector.

Because intraseasonal extratropical oscillations are known to be most active during NH wintertime (Knutson and Weickmann 1987; Ghil and Mo 1991a; PV94), earlier modeling studies assumed constant NH winter conditions. Strong et al. (1993) introduced an annual cycle in the forcing of their barotropic QG model. Their model is identical to Tribbia and Ghil's (1990), except that the hemispheric symmetry — present in LG and absent from Tribbia and Ghil's (1990) model — is preserved. An extratropical 40-day oscillation is still present in the seasonally forced QG model, with its activity essentially confined to the extended NH winter season: late fall, winter, and early spring. Strong et al. (1995) performed a linear stability analysis, using Floquet theory, of this model's annual cycle, averaged over many years of integration. Their results confirmed the 40-day oscillation's seasonal preference for winter.

The present study intends to bridge the gap between the barotropic QG and multi-layer GCM studies by using a two-layer primitive-equation model with realistic topography, while also examining the observed intraseasonal oscillations in a 13.5-year-long data set. Like Tribbia and Ghil's (1990) model and the UCLA GCM, this model avoids the possibility of Rossby-wave reflection from the equator by not assuming hemispheric symmetry. The two main departures from the QG simulations are the use of an ageostrophic, primitive-equation system and of a two-layer configuration that allows the dynamical effects of divergence to manifest themselves.

In order to focus on intraseasonal dynamics, we choose to suppress baroclinic instability by adopting a physically realistic density ratio of 0.5 between the upper and the lower layer, while retaining the incompressibility condition of the previous QG studies. The large effective static stability stemming from this formulation (see next section) damps the growth of baroclinic waves on synoptic

time scales, while the divergence field is allowed to interact fully with the large-scale, intraseasonal variability we wish to investigate. The damping of baroclinic waves is justified by our concentrating on low-frequency variability, which is dominated in the extratropics by barotropic dynamics (Wallace 1983; Wallace and Blackmon 1983; Lau and Nath 1987; Branstator 1995). Furthermore, the model used here has no parameterization of physical phenomena such as radiation, cloud formation, or precipitation; its internal mechanisms are thus strictly fluid dynamical and, as such, do not include the tropical-convection phenomena associated with the MJO (Madden and Julian 1971, 1972).

The paper is organized as follows. The model and its climatology are outlined and the data set is described in section 2. We provide in section 3 an overview of the time-series analysis methods to be used. A 13.5-year-long data set of NH atmospheric angular momentum (AAM) and a longer set generated by the model are submitted to spectral analysis in section 4. The spatial structure of the two-layer model's intraseasonal oscillations is then analyzed in section 5, in parallel with the corresponding observed oscillations. Section 6 concludes the paper with a brief summary and discussion of the results.

2 Model and data

a. Governing equations

The model is a more realistic version of the one developed by Keppenne (1989) to study the nonlinear dynamics of large-scale flows in the terrestrial atmosphere. A modified version was used by Keppenne (1992) and Keppenne and Ingersoll (1995) to investigate topographically forced barotropic modes in the Martian atmosphere.

The model is derived and discussed in detail by Haltiner and Williams (1980, pp. 54–59), among others. It is succinctly described by the following dimensionless system of prognostic equations:

$$\partial_t \Delta \psi_i = -\nabla \cdot \left[u_i (\Delta \psi_i + f) \right] - \tau \delta_{i2} U_2 \Delta \psi_i + (-1)^{n+1} \gamma \nabla^n \psi_i, \tag{1a}$$

$$\partial_t \Delta \chi_i = k \cdot \nabla \times \left[u_i (\Delta \psi_i + f) \right] - \tau \delta_{i2} U_2 \Delta \chi_i + (-1)^{n+1} \gamma \nabla^n \chi_i - \Delta \left[\frac{u_i \cdot u_i}{2} + \phi_2 + \alpha_i \phi_1 + \phi_b \right], \tag{1b}$$

$$\partial_t \phi_i = -\nabla \cdot u_i \phi_i - \bar{\phi}_i \Delta \chi_i - \varepsilon_i \Delta \left(\phi_i - \phi_i^* \right). \tag{1c}$$

In Eqs. (1a)–(1c), the subscript i takes the values 1 and 2 for the upper and lower layers, respectively; (1a, b) is the vorticity-divergence form of the momentum equation and (1c) is the mass-conservation equation. For each value of i, $\psi(\lambda, \theta, t)$, $\chi(\lambda, \theta, t)$, and $\phi(\lambda, \theta, t)$ are the corresponding layer's streamfunction, velocity potential, and the deviation of the geopotential height from its global average $\bar{\phi}_i$; λ is longitude, θ latitude, and t time. Time is rendered dimensionless by measuring it in units equal to Earth's rotation period, $2\pi/\Omega$, while the "dimensionless length unit" is Earth's equatorial radius. Each layer's horizontal fluid velocity is $u(\lambda, \theta, t)$, the Coriolis parameter is $f = 2\Omega \sin \theta$, τ is a drag coefficient, α the ratio of the upper layer's density to that of layer i (that is, $\alpha_1 = 1$, $\alpha_2 = \rho_1 / \rho_2$), γ is a diffusion coefficient, U the layer's mean-square-root zonal kinetic energy per unit mass, $\phi_b(\lambda, \theta)$ is topographic height and Δ the Laplacian operator. The forcing field $\phi^*(\theta)$ depends only on latitude in each layer; hence the relaxation term $-\varepsilon \Delta \left(\phi - \phi^* \right)$ is applied exclusively to the zonally symmetric component of each layer's geopotential field.

The upper limits of the two layers, each consisting of a homogeneous fluid with constant density, are placed near 5000 and 15000 meters ($\phi_2 = 9$ and $\phi_1 = 18$ in dimensionless units). These approximately correspond to the 500- and 100-mb levels of the U.S. Standard Atmosphere, so that our model's two layers are a physically realizable, albeit highly idealized, representation of the lower and upper troposphere. Layer models provide a useful intermediate step between barotropic models and the so-called "level" models, which apply finite-difference approximations directly to the equations of motion for a continuously stratified fluid; they typically employ a vertical density profile which mimics the potential temperature structure of the atmosphere (e.g. Weimer and Haken 1989, and references therein). This choice permits a layer model to simulate baroclinic processes (Pedlosky 1987), but the resulting vertical density gradients are unrealistically small; Ghil and Todling (1996), for example, used a density ratio of 0.95 in a two-layer model to study data assimilation on synoptic time scales and wished, therefore, to emphasize the role of baroclinic instabilities .

Since our interest is in longer time scales, which are dominated by barotropic effects in the extratropics (Wallace 1983; Lau and Nath 1987), we choose a more realistic value of $\alpha_1 = 0.5$ for the relative density of the upper layer in this study. The resulting low value for the rotational Froude number effectively suppresses baroclinic instability in our two-layer system [cf. Pedlosky 1987, Eq. (7.11.17)], thereby helping us focus on the large-scale, intraseasonal oscillations we wish to investigate. Choosing $n = 4$ yields a highly scale-selective diffusion term, in order to suppress small-scale noise, and the diffusion coefficient γ is $5 \cdot 10^{-12}$. A dissipation time scale of 10 days in the lower layer gives $\tau = 0.1$, and the relaxation time ε^{-1} is 15 and 10 days for the upper and lower layers, respectively.

Equation (1) is expanded in terms of spherical harmonics and its spectral form is integrated at rhomboidal truncation R15 using an associated Gaussian grid with 40 Gaussian latitudes and 48 meridians. This resolution is slightly cruder than that used in the UCLA GCM in its standard 4° latitude by 5° longitude configuration (Marcus et al. 1994, 1996). The transform method (Eliassen et al. 1970; Orszag 1970; Bourke 1972) is used to iterate back and forth between the gridpoint and spectral representations of the model variables. The spectral representation of (1) is integrated using a leapfrog scheme with semi-implicit treatment of the pressure gradient and divergence terms, allowing a time step of one hour. An Asselin (1972) time filter is applied to damp the spectrum of internal and external gravity waves in the initial phase of the integration. A modified Euler backward step (Kurihara 1965) is applied every 4 days to damp the computational mode associated with the leapfrog scheme.

The two layers' geopotential fields are forced with the December-January-February (DJF) 1963–1973 zonally averaged observed climatology [Oort 1983: $\phi^*(\theta)$ in Eq. (1c)]. Its intensity is enhanced by 25% to give time-averaged NH midlatitude jets of 30 and 15 ms^{-1} for the upper and lower layer, respectively. The main model simulation spans 105 years, of which the first five were discarded to ensure a stable climatology. Many shorter simulations with different parameter values have been carried out; only two such series of numerical experiments are described in this paper, for varying topographic heights and zonal forcing (see section 4).

b. Simulation of the wintertime climatology

The model's zonally averaged and time-mean fields compare favorably with the boreal-winter climatology of other multi-layer models -- such as the finite-difference UCLA GCM (Arakawa and Lamb 1977; Marcus 1990) and the pseudo-

spectral GCM of McAvaney et al. (1978) -- especially when considering the simplified dynamics employed here. The diagnostics discussed below were extracted from the 100-year model simulation using constant boreal-winter forcing $\phi^*(\theta)$ as described above.

i. Zonally averaged quantities

The zonally averaged time-mean zonal wind is shown in Fig. 1a. Westerly jet maxima of about 25 and 30 ms^{-1} in the upper layer obtain for the southern and northern hemispheres, respectively. The overall distribution and intensities of tropical easterlies and midlatitude westerlies is well captured in the simulation. The tropospheric wind maximum in the NH is reasonably well positioned for the boreal winter, although it is shifted northward by about 5° with respect to the observations (cf. Grotjahn 1993, Fig. 3.15 there).

Figure 1b shows the time-mean zonally averaged geopotential height for the model's upper and lower layers. The profiles look similar to those observed for NH wintertime conditions (cf. Grotjahn 1993, Fig. 3.21 there).

[Fig. 1 near here, please]

ii. Streamfunction and zonal wind

Figure 2a shows the model's NH time-averaged barotropic streamfunction. A dominant wavenumber-two configuration extends over the NH extratropics, with troughs slightly east of the American and Asian continents, and ridges slightly west of Europe and North America; a weaker trough-ridge system located over Eurasia shows the presence of higher zonal wavenumbers. The southern hemisphere flow

9

(not shown) is relatively zonal due to lack of large-scale surface forcing in this hemisphere.

[**Fig. 2 near here, please**]

The time-mean zonal wind component in the upper layer (Fig. 2b) exhibits strong, elongated maxima in the model's westerly winds, associated with the jet stream over the NH extratropics. Evident are the two jet exit regions over eastern Asia and the east coast of the United States; the successful simulation of these features in our simplified model emphasizes the importance of topographic vs. thermal forcing in their generation (Charney and Eliassen 1949; Smagorinsky 1953; Held 1983). The zonal wind component over the southern hemisphere (not shown) is more zonally uniform.

iii. Streamfunction variability

Figure 3 shows maps of the standard deviation of the model's upper-layer streamfunction. To separate the contributions from the model's low- and high-frequency variability, the standard deviations are shown separately for 5-day mean fields (Fig. 3a) and deviations from the 5-day means (Fig. 3b), respectively. The spatial patterns of low-pass variability — which forms the subject of our investigation — are realistic, although the amplitude of the stationary waves (see Fig. 2a) is underestimated with respect to the observations (see Kalnay et al. 1996 for the reanalysis procedure and http://www.cdc.noaa.gov/cdc/reanalysis/ for the relevant maps). The three well-known low-frequency maxima over the northeastern Pacific and Atlantic basins and over northern Siberia are reproduced (Fig. 3a).

The simulation shows reasonable agreement with observed features at high (i.e. synoptic) frequencies, although the storm tracks are positioned too far north on the eastern North American and Asian coasts, with maxima confined to areas near the continental margins. The lack in Fig. 3b here of the observed (Lau 1988) seaward extensions of the storm tracks in the direction of the Kuroshio and Gulf Stream currents emphasizes the importance of zonally nonuniform thermal forcing (absent from our simplified model) for their maintenance. The southern hemisphere flow (not shown) exhibits a nearly zonal band of variability associated with the circumpolar trough in that hemisphere.

c. Observational data set

The data set consists of daily analyzed fields of global wind and streamfunction at 200-mb from 1 January 1980 to 31 July 1993. From January 1980 to February 1984, the analysis was performed by the European Centre for Medium-Range Weather Forecasts, and thereafter by the Japan Meteorological Agency. The spatial resolution of the data is 2.5° longitude by 2.5° latitude. The average seasonal cycle, defined by the first four annual harmonics of the 13.5-year time series, was removed from the data prior to computing the AAM.

The data set's NH AAM is computed from the 200-mb zonal wind averaged north of 30°N, for two reasons: (i) It is known that the "wind term" dominates the "pressure term" in the intraseasonal AAM budget (Dickey et al. 1991; Hide and Dickey 1991; Marcus et al. 1994); and (ii) 30°N corresponds fairly closely to the nodal line of streamfunction anomalies associated with the intraseasonal variability. The latter choice allows us to focus on the purely extratropical component of

observed variability, which the model may or may not capture, and eliminate the purely tropical aspects of this variability, such as the MJO, which the model is not intended to simulate at all.

3.   Time-series analysis methods

Several modern approaches to frequency- and time-domain analysis form the basis for the present study's model and observational diagnostics. Single-channel singular-spectrum analysis (SSA: Vautard et al. 1992), the maximum entropy method (MEM: Penland et al. 1991), and the multi-taper method (MTM: Thomson 1982) are applied using the "SSA Toolkit" developed by Dettinger et al. (1995a). The latest version of the toolkit, now called the SSA-MTM Toolkit, is available as freeware at http://www.atmos.ucla.edu/tcd. More complete methodological reviews are given by Ghil and Yiou (1996), Yiou et al. (1996), and Ghil and Taricco (1997).

a. Maximum entropy method (MEM)

Traditional methods of power spectrum estimation, based on the Fourier Transform (FT) of an autocorrelation function (correlogram) or of the time series itself (periodogram) have long been used to identify the frequencies at which significant power is present in a given time series. In addition to these techniques, we use sharper — and complementary — power spectrum estimation methods to extract weak oscillations from noisy series, along with more sophisticated statistical-significance tests.

Blackman-Tukey (BT) or correlogram approaches (Blackman and Tukey 1958) to spectral analysis describe a time series' power spectrum as

$$P(f) \sim \sum_{k=1}^{N} \rho(k) w(k) e^{ikf\Delta} ; \qquad (2)$$

here f is frequency, $P(f)$ the spectral density at a given frequency, $\rho(k)$ the autocorrelation for lag k, $w(k)$ a weighting function, and Δ is the sampling interval, $\Delta = T / N$, with T the length of the time series and N the number of data points. In contrast, MEM is based upon the approximation of noisy periodic signals by autoregressive (AR) processes driven by white noise. This alternative approach relies on representing the power spectrum as

$$P(f) = \frac{a_o}{\left| 1 + \sum_{k=1}^{M'} a_k e^{2\pi ikf\Delta} \right|^2} , \qquad (3)$$

where $\{a_k, k = 1,...,M'\}$ are the AR coefficients of the original time series (Childers 1978; Press et al. 1992), and a_o denotes the noise level. By the Wiener-Khinchin theorem, $P(f)$ in Eq. (3) equals the FT of the autocorrelation function for the approximating AR process. This property allows Eq. (3) to be fitted based on sample autocorrelations up to a lag $M \geq M'$.

MEM spectral estimation is of interest in two ways: 1) the power spectrum can contain up to $M' \leq M$ poles, that is, singularities where the denominator in Eq. (3) goes to zero, and 2) the power spectrum is not forced into the regular mold of a Fourier series, with power only estimated at multiples of a basic frequency $2\pi / T$. The former aspect of MEM allows a more complete description of narrow spectral

peaks, effectively giving a higher resolution. The latter aspect of MEM allows a more data-adaptive description of the overall power-spectrum form.

The number of poles, M', used in MEM requires some caution. Generally, one wants to limit this value to a small multiple of the expected number of sharp spectral features. Higher-order MEM fits tend to produce spurious peaks (Penland et al. 1991), in addition to the actual lines in the given time series. Therefore, MEM results should be judiciously compared against those obtained from BT methods, and those of the MTM, described next.

b. Multi-taper method (MTM)

This method, due to Thomson (1982), supplements the BT and MEM spectral estimates by locating sharp lines in a time series' power spectrum. It yields, in principle, arbitrarily high resolution, and provides a statistical Fisher test (F-test) for the validity of each peak in the resulting spectrum, and for its amplitude.

The method is based on the theoretical work of Slepian (1978) and is designed, given a time series

$$x_j = \mu \sin(2\pi j f_0) + \xi_j, 1 \le j \le N,$$ (4)

where μ represents amplitude, f_0 a line frequency and ξ a white-noise process, to minimize the power leakage of f_0 outside a pre-determined frequency band B,

$$B = (f_0 - W, f_0 + W)$$ (5)

by tapering the signal according to

$$x_j v_j, 1 \le j \le N. \tag{6}$$

The multiple tapers $\{v(j), j = 1,...,N\}$ are optimally produced using the leading K discrete prolate spheroidal sequences (DPSSs), often called Slepian sequences for short. The tapers are specifically designed to optimize the estimate of line frequencies f_0 and their corresponding amplitudes μ by least-squares regression. The bandwidth W is typically chosen to be on the order of $4/N$ to $16/N$, where N is the number of equidistant points, as before. For a given W and N, the leading $K = 2NW$ DPSSs have the best spectral properties and are generally used in MTM. A more complete, but still concise review is given by Ghil and Yiou (1996); Percival and Walden (1993) provide an extensive treatment.

The resulting estimate of amplitudes contains a ratio of explained to unexplained variance at each frequency f, which can be subjected to an F-test to test the null hypothesis $\mu = 0$ with the lowest probability of failure; $\mu = 0$ implies that the series is white. The method, therefore, can detect with a high degree of confidence low-amplitude oscillations, whose validity is only poorly estimated or missed entirely by other methods. By way of illustration, the BT method has error bars proportional to the amplitude of the spectral peaks, while MEM estimates of error bars (Baggeroer 1976) are difficult to calculate in general (Penland et al. 1991).

Still, a large number of MTM peaks tend to pass the F-test with high confidence in a white- or red-noise process (Vautard et al. 1992). Mann and Lees (1996) have devised a two-stage algorithm for ascertaining that the peaks are only deemed significant if they exceed, in the second stage, the amplitude associated with a red-noise background determined in the first stage. We use the F-test results of Thomson's (1982) version of MTM only if corroborated by the results of another

spectral method, such as MEM with a judiciously chosen order (Ghil and Yiou 1996; Ghil and Taricco 1997); see discussion of Fig. 4 below.

c. Single- and multi-channel singular-spectrum analysis (SSA and M-SSA)

SSA is a nonparametric method designed to extract as much reliable information as possible from short time series without prior knowledge of the dynamics underlying the series. The method is a form of empirical orthogonal function (EOF) analysis of lagged data, for lags $k, 1 \leq k \leq M$, where $M\Delta$ is the window width. It provides data-adaptive linear filters for separation of a time series into statistically independent components, with no prior assumptions about their functional form. In principle, SSA can be used to infer the statistical dimension of short, noisy time series and thereby place upper bounds on the dynamical dimension of the underlying physics (Vautard and Ghil 1989). The extension to multiple channels, M-SSA, accounts for lagged cross-correlations between pairs of spatial variables. Technical SSA and M-SSA details have already been described elsewhere (e.g., Vautard and Ghil 1989; Ghil and Mo 1991a; Vautard et al. 1992; PV94), so we will only briefly summarize the main aspects below.

Vautard and Ghil (1989) showed that periodic components give rise in SSA to paired eigenvalues. That is, a periodic component in a time series will be represented by two temporal empirical orthogonal functions (T-EOFs) with nearly equal eigenvalues, and in phase quadrature with each other. Typically, both T-EOFs are necessary to retrieve the period as well as the phase of the components, so the (M-)SSA splits the variance equally between the two corresponding eigenvalues. Equal eigenvalues lead to indeterminacy in the solution of eigenproblems and thus are troublesome in traditional, spatial EOF analysis (Preisendorfer 1988). In contrast, in this temporal EOF analysis, while spurious degeneracy of eigenvalues is still

possible, periodic components can be tested for with relative ease by considering frequency and quadrature criteria (Dettinger et al. 1995a; Ghil and Taricco 1997, and references there).

The adaptive filtering provided by (M-)SSA has the pleasing property that oscillations with small frequency variations are identified and reconstructed as a single oscillation, rather than as several separate signals as in MEM and MTM. BT methods, on the other hand, while also providing broad peaks, might require more than one frequency — that is, both the fundamental and some of its harmonics — to describe anharmonic, nonlinear oscillations.

Finally, one may reconstruct a filtered time series based on any subset of modes. The leading temporal principal components (T-PCs) decompose the major, organized variance of the signal and allow for the identification of elementary processes (Yiou et al. 1994). However, the T-PCs are ambiguous as to epoch — they do not allow for the precise timing of oscillation spells and are, furthermore, of length $N - M + 1$. Ghil and Vautard (1991) recovered the exact phase of a filtered signal by reconstructing it from the convolution of one or several of the T-PCs with the corresponding T-EOFs, thus recasting the result into the original time domain $0 \leq j \leq N$. The resulting time series for a single T-PC is called a reconstructed component (RC), and the RCs have additive properties — that is, the sum of all RCs gives back exactly the original time series. Vautard et al. (1992) provide more technical details on the RCs [their Eqs. (2.17a–c)]. The present study incorporates both univariate and multivariate RCs, since they are useful in timing precisely the intermittent nature of the intraseasonal activity.

4 AAM variability in the model and observations

Atmospheric angular momentum (AAM) is by definition a wavenumber-zero quantity and represents one of the most basic diagnostics of atmospheric behavior. Its variability on the intraseasonal time scale induces changes in the Earth's rotation rate of a few tenths of milliseconds (Eubanks et al. 1985; Marcus 1990). This AAM variability is associated with planetary-scale wave activity (Madden 1988; Jin and Ghil 1990; Ghil and Mo 1991a), and is of interest in space geodesy (Hide and Dickey 1991; Keppenne and Ghil 1993).

a. MEM and MTM results

In Figs. 4a, b, we show combined MEM-MTM power spectra by latitude belt of the model and observed AAM, respectively. For both figures, the sampling rate Δ is 3 days, and the MEM order M' is equal to 60; higher values of M' tend to produce spurious peaks, while lower M' values eliminate finer features of the spectra (Penland et al., 1991; Vautard et al., 1992). The MEM spectra in the figures are represented by light solid contours, with shading used for the greatest power. The power at each latitude has been multiplied by the frequency, so that equal areas in a plot of power vs. logarithm of the frequency at each latitude (not shown) correspond to equal integrated power (cf. Dickey et al. 1991). The MTM peaks which survived an F-test with a 99.5% threshold are plotted as heavy open circles, to complement the MEM spectra.

[Fig. 4 near here, please]

The model's MEM spectra (Fig. 4a) are dominated by NH mid-latitude variability with a time scale of 35-40 days, while for the observational spectra (Fig. 4b) the dominant signal arises in the tropics with a period near 50 days. The latter is believed to be a signature of the MJO (e.g., Benedict and Haney 1988), which is driven by regional latent heating interacting with a planetary-scale, eastward-propagating wave instability (e.g., Lau and Peng 1987). Its complete absence in our two-layer model is consistent with its dynamics-only formulation (see section 2), which does not include convective or diabatic processes; Slingo et al. (1996) have noted that even full-physics GCMs that use sophisticated convective schemes often fail to achieve a robust simulation of the MJO.

In addition to the tropical oscillation, the observed spectra also show enhanced power in the NH extratropics, with periods similar to that of the dominant model oscillation. The MTM spectra, in particular, clearly delineate separate tropical and extratropical oscillations in the observed AAM data, with periods near 50 and 40 days, respectively. The presence of an extratropical oscillation with roughly the same period in our dynamics-only model suggests that the observed 40-day oscillation may also have a dynamical origin, independent of the convective forcing that generates the 50-day oscillation in the tropics.

Another low-frequency oscillation is active in the NH low- to mid-latitudes in the observations, where its mean period is near 70 days (MEM and MTM results in Fig. 4b). The model's spectra (Fig. 4a) show no low-latitude variability associated with this oscillation, only a strong 65–70-day signal in NH mid- and high-latitudes. The flow patterns associated with both of these oscillations in the model will be compared to observations in the next section.

b. SSA results

We apply SSA to the univariate time series of the NH AAM to facilitate understanding the temporal evolution of the intraseasonal oscillations. For the observed data, an initial application of SSA with $M\Delta = 200$ days was used to reconstruct and remove variability longer than the intraseasonal range of 100 days. Subsequently, a window width of $M\Delta = 120$ days was applied to both model and observed NH AAM, resulting in the log-eigenvalue spectra of Figs. 5a, b for the model and observations, respectively.

[Fig. 5 near here, please]

The model exhibits a spectrum having eight leading eigenvalues, an intermediate slope, and a break to a noise floor after index 21. The leading eigenvalues 1–2, 3–4, 5–6, and 7–8 are oscillatory pairs, judging by Ghil and Mo's (1991a) very conservative (compare Dettinger et al. 1995b) error-bar estimates. The observed AAM — having subtracted the mean annual cycle, as well as the residual variability longer than 100 days — shows a similar eigenvalue spectrum (Fig. 5b). The eigenvalue pairs 1–2, 3–4, 5–6, and 7–8 all represent intraseasonal oscillations, except that the last two pairs, eigenvalues 5–8, are less well separated from each other in the shorter observed record. Varying the window width — to equal 75, 100, or 150 days — does not alter the existence of the oscillatory pairs, but does change the relative number of eigenvalues present in the intermediate slope and the tail of the spectra. The latter change is consistent with the theoretical results of Vautard and Ghil (1989); see also Yiou et al. (1994).

In both model simulation and observed data, the first two T-EOFs capture the 70-day oscillation, and account for 28% and 22% of the variance, respectively. The

pair 3–4, accounting for 20% of the modeled and 17% of the observed variance, contains the 40-day extratropical oscillation. Although less well-defined, T-EOFs 5–6 capture the 23-day activity in the model time series, while for the observed AAM, T-EOFs 5–6 and 7–8 capture a 27- and 23-day oscillation, respectively. The 23-day oscillation has 14% of the variance in the model AAM, while the 23- and 27-day oscillations together account for 16% of the variance in the observed AAM.

Reconstruction of filtered time series from modes 1–6 for the model and 1–8 for the observations recovers the intraseasonal contributions to the AAM time series (Figs. 6a and b for model and observations respectively), while leaving out the high-frequency "noise" — i.e., variability at synoptic and shorter time scales — as well as trends and lower-frequency oscillations, if any. For ease of comparison with the data, only a 13.5-year-long segment of the model simulation is shown; other equal-length segments give similar results (not shown). In both time series, the largest variations in AAM are associated with the 70-day mode, with the 40-day oscillation supplying the next largest signal. In the observations it is clear that the most vigorous intraseasonal activity occurs in the extended winter, with large-amplitude, sustained oscillations visible in 1982–83, 1986–87, and 1989–90 (Fig. 6b; see also Dickey et al. 1991; Ghil and Mo 1991a). The model's perpetual-winter NH AAM time series (Fig. 6a) also shows distinct spells of intraseasonal activity (compare Marcus et al. 1994 and Strong et al. 1993, 1995).

[Fig. 6 near here, please]

These findings are consistent with recent modeling and observational results concerning the extratropical 40-day oscillation. The 70-day oscillation, however, had not been detected in the earlier studies that used barotropic QG models. It is not

clear at this point whether it is the present model's two-layer configuration or primitive-equation formulation that contribute most to its successful simulation here. To elucidate this question, we also ran a single-layer version of the model for 18 years, discarded the first three years thereof, and analyzed the remaining 15 years of AAM history. A 70-day signal was still identified in this version of the model, suggesting that the primitive-equation system, incorporating the effect of topography (see below) helps capture it, while the two-layer configuration is not as important.

This conclusion is rather tentative, since Itoh and Kimoto's (1998) linear-balance model also exhibits a NH 50–70-day oscillation at a comparable horizontal resolution (T21 rather than R15) and with five vertical levels. Their spatial pattern does not agree so well, however, with the 70-day pattern shown in section 5 below.

c. Sensitivity tests

The model results were tested for sensitivity to topographic height and geopotential forcing strength. For the first test, the model's forcing ϕ^* was held constant in Eq. (1c), while a nondimensional topographic height parameter h was introduced, replacing ϕ_b in Eq. (1b) by $h\phi_b$, with h ranging from 0.1 to 1.0. Applying an F-test of 99% to the MTM spectra (not shown) of the corresponding 15-year time series of NH AAM shows no significant peaks for $h = 0.1$ or 0.3; in fact, intraseasonal oscillations of period longer than about 30 days only appear for $h \geq 0.6$. The present results agree with the UCLA GCM experiments of Marcus et al. (1994, 1996), who found a robust 40-day oscillation in their perpetual-winter experiment with realistic topography, but no intraseasonal oscillations whatsoever in their three zero-topography experiments. A 40-day oscillation is found to be statistically significant, albeit with slightly different periods, for $0.6 \leq h \leq 1.0$.

The 70-day oscillation has nearly identical periods for $h = 0.9$ and 1.0 and is not significant in the $h = 0.8$ experiment; a slightly lower-frequency, 74–80-day oscillation is present, however, for $h = 0.7$ and 0.6. It is also interesting to note that an oscillation of mean 23-day period is significant in all experiments for which $0.5 \leq h \leq 1.0$.

In the second sensitivity experiment, the model's topography ϕ_b was held constant in Eq. (1b), while a nondimensional forcing parameter σ was introduced, replacing ϕ^* in Eq. (1c) by $\sigma\phi^*$. For reduced forcing, $\sigma = 0.75$, the number of statistically significant spectral peaks is smaller (not shown). This is consistent with the overall lack of intraseasonal oscillations in the NH extratropics during boreal summer, as documented by Strong et al. (1993, 1995), among others. When the forcing is higher — $\sigma = 1.25$ and 1.5 — a larger number of significant peaks cluster in the 15–30-day range than for periods of 40 days or longer. These results agree well with Strong et al.'s (1993) model study, in which higher forcing systematically favored shorter-period variability (their Figs. 9a and 9b).

5 Spatial patterns of intraseasonal variability

We examine now the spatial patterns associated with the oscillations that were identified objectively by their spectral properties in Figs. 4 and 5. To do so, we composite maps of the upper layer's streamfunction-anomaly field, keyed to the extrema and zero crossings of an SSA-filtered time series which isolates each oscillation in the total NH AAM from the remaining variability (see Figs. 6a, b). The close connections between the scalar AAM time series and the multivariate time series of upper-air fields of streamfunction and geopotential have been

demonstrated by Ghil et al. (1991) and Marcus et al. (1996) for the UCLA GCM and by Strong et al. (1993, 1995) for a barotropic QG model.

The model's streamfunction anomalies are obtained by M-SSA, which isolates the same intraseasonal oscillations that are present in the AAM. These multivariate RCs, keyed to the filtered AAM, provide a dynamical link between the complex spatial patterns and the evolution of a univariate quantity (see also Kimoto et al. 1991; Keppenne and Ghil 1993; PV94; Dettinger et al. 1995b; Jiang et al. 1995). The compositing is based on the streamfunction field to match the compositing in the observed data set.

For the observed streamfunction, spatial patterns associated with the oscillations are investigated by compositing the fields at 200 mb keyed to the NH AAM time series reconstructed from the oscillatory pairs. For each oscillation, different bandpass filters are applied to obtain the streamfunction anomalies. A degree-4 Butterworth filter (Rabiner and Gold 1975) with half-power points at 50 and 120 days is used for the composites of the 70-day mode; for the 40-day mode, a 25–75-day bandpass filters is used.

The compositing criteria, common to both the model and observations are:

- For maximum and minimum phases, the absolute value of the (reconstructed) AAM anomaly should exceed a threshold of 2.0 times the standard deviation of the reconstructed time series.

- For transition phases, that is, AAM decreasing or increasing, we first identify a date of zero-crossing, then check backward and forward in time from this date to find the dates of immediately preceding and succeeding categories that are appropriate; that is minimum and maximum phases. Next, the absolute values of the (reconstructed) AAM anomaly for both of these extreme phases are required to be larger than 1.6 times the standard deviation of the time series.

Finally, either one of the two is required to have a value in excess of 2.0 times the standard deviation, in order for the transition dates to be included in the compositing.

The number of maps that pass the compositing criteria and were used for the observed 40-day oscillation equals 18, 16, 20, and 16 for the maximum, decreasing, minimum, and increasing phases, respectively. For the 70-day oscillation in the observed data set the corresponding numbers are 13, 16, 17, and 15.

a. 40-day oscillation

The streamfunction-anomaly composites of Figs. 7 and 8 describe successive phases of the 40-day oscillation for the model and observations, respectively. The composites in either figure are keyed to the SSA-filtered time series that isolates the anharmonic oscillation being examined from the remaining NH AAM variability.

[Figs. 7 and 8 near here, please]

The composites in both Figs. 7 and 8 show a standing midlatitude pattern reminiscent of those identified in some of the QG studies (Jin and Ghil 1990; Tribbia and Ghil 1990; Strong et al. 1993) and in the UCLA GCM (Marcus 1990), with a strong wavenumber-two component poleward of 40°N. The pattern is more pronounced in the extreme phases of the AAM cycle than in the transition phases; it has a higher "signal-to-noise" ratio in the model composites, which comprise a greater number of individual maps than are available in the more limited observational sample. Two arches of an extratropical wave train, one over the North Pacific and North America and the other over northern Europe and Eurasia, are

characteristic of this mode. The centers of maximum amplitude are located in the Pacific/North-American (PNA) sector, followed by the Eurasian sector (see also the observational results of PV94 and the GCM results of Marcus et al. 1996). The pattern correlation between the model and observed composites is best over the PNA sector; its value there, when averaged over the four phases, is 0.74.

The ridges and troughs of the dominant wavenumber-two pattern here, like those in the UCLA GCM (Ghil et al 1991; Marcus et al. 1996), tilt southwest-to-northeast in the oscillations' low and high phases (Figs. 7a, c and 8a, c). In the transition phases (Figs. 7b, d and 8b, d), the ridges and troughs shift to a southeast-to-northwest tilt. The successive alignment of the height gradients parallel to and across the underlying topographic features, especially over the Rockies, gives rise to the alternating mountain torque which has been ascertained to drive the AAM oscillation in the UCLA GCM (Marcus 1990; Ghil et al. 1991). The appearance of similar patterns here in the two-layer model composites (Fig. 7) and the observations (Fig. 8) indicates that it is a robust feature of the extratropical 40-day AAM oscillation over the PNA sector. This tilted-trough vacillation is characteristic of barotropic energy conversions and suggests a connection with the "classical" index cycle of intraseasonal variability in the intensity of the mid-latitude westerlies (Rossby et al. 1939; Namias 1950; Lorenz 1963; Ghil and Childress 1987, pp. 126, 170, 201).

The vacillation is accompanied by a meridional mass transfer between the mid-latitude wavenumber-two oscillation and a zonally symmetric oscillation in the tropics. This "sloshing" (not shown) is similar to the zonally symmetric component of the 40-day oscillation seen in the UCLA GCM (Ghil et al. 1991; Marcus et al. 1994), and is required to preserve the geostrophic and equivalent-barotropic structure of the model oscillation. Composites of the extratropical 40-day oscillation in observed

data have also been examined by Kimoto et al. (1991) and PV94. They showed a standing wavenumber-two oscillation similar to the one found in each of the model's two layers and the observational data set here.

b. 70-day oscillation

The composites illustrating the 70-day oscillation in the model and observations are shown in Figs. 9 and 10, respectively. Again, these composites are keyed to univariate SSA-filtered series, which carry the variability associated with the oscillation in the model or observed NH AAM, respectively. In this case, however, the M-SSA analysis did not separate pairs of T-PCs corresponding to the 70-day oscillation when using the entire NH grid of the model. A more limited M-SSA application — suggested by the work of PV94 — to the model's Euro-Atlantic sector (30° to 90°N and 80°W to 40°E) did produce a pair of T-PCs corresponding to the 70-day oscillation in AAM. The 70-day oscillation appears therewith to be less hemispheric in character than the 40-day mode of the preceding subsection.

[Figs. 9 and 10 near here, please]

Figure 9 describes the successive phases of the 70-day model oscillation over the Euro-Atlantic sector. The main feature of this oscillation in its extreme phases is a north-south dipole structure that strengthens the Atlantic jet stream in the maximum AAM phase and weakens it in the minimum AAM phase. It is thus similar to the Greenland-northern Europe "seesaw" of Van Loon and Rogers (1978).

In observations keyed to the full NH AAM, the 70-day mode's extreme phases (Figs. 10a, c) are characterized by a similar north-south Atlantic dipole, also accompanied by a Greenland-northern Europe "seesaw." These patterns bear a

27

strong similarity to a seasonal composite of the North Atlantic Oscillation (NAO) constructed by Hurrell (1995) using wintertime 300-mb streamfunction anomalies (his Fig. 9). Its marked resemblance to our model's high-AAM composite (Fig. 9a), in particular, and to the model's low-AAM composite (Fig. 9c) with the sign of the anomalies reversed, indicates that the NAO operates on intraseasonal as well as interannual time scales.

In addition to oscillations in the Atlantic sector, our observational composites also show north-south dipoles over the Pacific and Eurasia. These features bear a strong qualitative resemblance to the second EOF found by Cheng and Wallace (1993) in their analysis of 10-day low-pass filtered NH wintertime 500-mb height data, and to patterns found by Kimoto (1987) and Kimoto and Ghil (1993a) in a similar analysis of a 700-mb data set. In all three data sets, 200-mb streamfunction fields here, 700-mb heights in M. Kimoto's work, and 500-mb heights in Cheng and Wallace's, the features of interest contain elements of both the North Atlantic and North Pacific Oscillations: compare Fig. 10a here with Fig. 6b of Kimoto and Ghil (1993a) and Fig. 10c here with Fig. 1b of Cheng and Wallace (1993). Evidently, the largest AAM oscillations occur when north-south fluctuations have the same phase in the Atlantic, Pacific, and Eurasian sectors (Figs. 10a, c).

6 Summary and discussion

Among the various phenomena responsible for observed atmospheric variability, we have made a distinction between fluid-dynamical and thermodynamical phenomena — such as the physics of the hydrologic cycle and cloud-radiation interactions — and have used a two-layer shallow-water system to

model the former. Our work continues a series of modeling and observational studies of Northern Hemisphere (NH) intraseasonal variability. It is intended to bridge the gap between the general circulation model (GCM) results of Marcus (1990) and Marcus et al. (1994, 1996) and those obtained with barotropic quasi-geostrophic (QG) models (Legras and Ghil 1985; Jin and Ghil 1990; Tribbia and Ghil 1990; Strong et al. 1993, 1995). Our model findings are verified against an observed record to present as complete a dynamic-synoptic description of the NH's intraseasonal variability as possible. This study, like the earlier ones, focuses on the NH's intraseasonal variability since data sets for the Southern Hemisphere are more limited [see, however, Mo and Ghil (1987) and Vautard et al. (1990)].

The incompressible, two-layer configuration we adopted permits fluid-dynamical interactions which were not possible in the earlier QG models, through the addition of a prognostic equation for the divergent velocity field. At the same time the choice of a realistic fractional density (0.5) for the upper layer acts to suppress baroclinic instability, active mainly on synoptic time scales, by maintaining a subcritical value for the model's rotational Froude number (see section 2). The model could thus isolate large-scale, intraseasonal oscillations of fluid-dynamical origin — including those that involve topography — from higher-frequency variations associated with unstable cyclone-scale waves, and from phenomena, such as the Madden-Julian (1971, 1972) oscillation (MJO), which are believed to involve coupled dynamical-thermodynamical mechanisms. By contrasting results obtained with the single-layer and two-layer versions, we could also see which model aspect — its multi-layer configuration or the presence of ageostrophic, divergent flow — seems to favor the simulation of a given intraseasonal oscillation.

Spectral analysis of a 100-year long time series of model-simulated atmospheric angular momentum (AAM), and comparison with a similar analysis of observed

AAM (Figs. 4a and b) lead to the identification of NH intraseasonal oscillations with average periods near 65–70 and 35–40 days. AAM time series filtered by singular-spectrum analysis (SSA) were used to further compare the model's oscillations with the observed ones (Figs. 5, 6). The 70-day oscillation is present in the observations (see also PV94) and in both the one- and two-layer versions of the model. Its absence from the results of QG studies suggests that it involves changes in the flow's ageostrophic, divergent component that do appear in the shallow-water model.

The 40-day oscillation appears in both versions of the model, as well as in QG models (Legras and Ghil 1985; Jin and Ghil 1990; Tribbia and Ghil 1990; Strong et al. 1993) and in the observed data set of 200-mb streamfunction used in this study. It has been reported in other observational studies as well (e.g., Weickmann et al. 1985; Dickey et al. 1991; Ghil and Mo 1991a; Kimoto et al. 1991; PV94). Its presence here is consistent with Ghil's (1987) hypothesis that the midlatitude 40-day oscillation is caused by the unstable interaction of the meandering westerly jet with NH topography.

As a matter of fact, topography plays a role in the excitation of all intraseasonal model oscillations: the flow evolves toward a quasi-steady state in equilibrium with the zonally symmetric forcing when the model is run without topography. A sensitivity study of model results to the topographic height and geopotential forcing points to their importance in initiating or maintaining the intraseasonal oscillations. The experiments with lowest topography showed no intraseasonal oscillations in the 30–100-day band. The forcing experiments in the presence of standard topography indicate that lower forcing -- identified with the weaker pole-to-equator temperature gradient that characterizes the summer hemisphere -- produces fewer intraseasonal oscillations, while higher forcing produces a greater number of shorter-period oscillations (see also Strong et al. 1993).

To study the spatial variability of each oscillation, we examined composites of the two-layer model's streamfunction-anomaly fields and those of the 200-mb data set and compared them with composites from other investigations. Like those found in earlier studies — modeling (Legras and Ghil 1985; Jin and Ghil 1990; Marcus 1990; Tribbia and Ghil 1990; Strong et al. 1993; Marcus et al. 1994, 1996) and observational (Ghil and Mo 1991a; Kimoto et al. 1991; PV94) — our composites of the 40-day oscillation (Figs. 7 and 8) show a standing wavenumber-two pattern with centers of actions located to the east and west of the North American and Eurasian continents' main topographic features. Its tilted-trough vacillation is analogous to the equivalent-barotropic phenomenon observed in rotating, differentially heated annulus experiments (Hide and Mason 1975; Lorenz 1963; Ghil and Childress 1987, Ch. 5), and is most robust in the PNA sector.

The 70-day oscillation, on the other hand, has its clearest signal in the Euro-Atlantic sector (Figs. 9 and 10), where it bears a strong resemblance to winter-season composites of interannual variability in the NAO (Hurrell, 1995). PV94 used M-SSA to study intraseasonal fluctuations in a 32-year set of NH extratropical 700-mb height data, and found that the leading mode had a period near 70 days, and was dominated by a spatial EOF resembling the NAO pattern of Wallace and Gutzler (1981). Our two-layer model, therefore, has the capability to reproduce the major features of these two oscillations in those portions of the NH extratropics which they dominate, i.e. the PNA and Euro-Atlantic sectors for the 40- and 70-day oscillations, respectively.

Our results thus imply that intraseasonal variability over the key NH extratropical centers of action has mostly fluid-dynamical, as opposed to thermodynamical causes. The 40-day oscillation is confirmed to have an independent origin in the NH extratropics, associated with tilted-trough vacillation

in the PNA sector, and is clearly distinct from the convectively-driven MJO, whose separate 50-day signal is evident in the tropics.

The 70-day oscillation in the Euro-Atlantic sector appears linked to ageostrophic, divergent motions in the shallow-water model, and their interaction with topography. Its close resemblance to observed NAO composites suggests that the latter's intraseasonal variability is driven not by thermal or baroclinic-eddy forcing, but arises instead from the large-scale dynamical processes captured in our simplified two-layer model, particularly topographic instability.

Further investigations using models with higher horizontal and vertical resolution, as well as longer and more detailed observational data sets, will be needed to clarify the manner in which topographic forcing acts to destabilize large-scale flows on intraseasonal time scales, and to identify the role of the resulting oscillations in modifying extratropical weather during boreal winter.

References

Arakawa, A., and V. R. Lamb, 1977: Computational design of the basic dynamical processes of the UCLA general circulation model. *Methods of Computational Physics*, **17**, Academic Press, 173–265.

Asselin, R., 1972: Frequency filter for time integrations. *Mon. Wea. Rev.*, **100**, 487–490.

Baggeroer, A. B., 1976: Confidence intervals for regression (MEM) spectral estimates. *IEEE Trans. Inf. Theory*, **IT-22**, 534–545.

Benedict, W. L., and R. L. Haney, 1988: Contribution of tropical winds to subseasonal fluctuations in atmospheric angular momentum and length-of-day. *J. Geophys. Res.*, **93**, 15973-15978.

Blackman, R. B. and J. W. Tukey, 1958: *The Measurement of Power Spectra from the Point of View of Communication Engineering*. Dover Publications, 190 pp.

Bourke, W., 1972: An efficient, one-level, primitive-equation spectral model. *Mon. Wea. Rev.*, **100**, 683–689.

Branstator, G., 1987: A striking example of the atmosphere's leading traveling pattern. *J. Atmos. Sci.*, **44**, 2310–2323.

———, 1995: Organization of storm track anomalies by recurring low-frequency circulation anomalies. *J. Atmos. Sci.*, **52**, 207–226.

Charney, J. G., and A. Eliassen, 1949: A numerical method for predicting the perturbations of the middle latitude westerlies. *Tellus* **1**, 38–54.

Cheng, X., and J. M. Wallace, 1993: Cluster analysis of the northern hemisphere wintertime 500-hPa height field: Spatial patterns. *J. Atmos. Sci.*, **50**, 2674–2696.

Childers, D. G. (Ed.), 1978: *Modern Spectrum Analysis*, IEEE Press, New York.

Dettinger, M. D., M. Ghil, C. M. Strong, W. W. Weibel, and P. Yiou, 1995a: Software expedites singular-spectrum analysis of noisy time series. *Eos, Trans. AGU*, **76**, no. 2, pp. 12, 14, and 21.

Dettinger, M. D., M. Ghil, and C. L. Keppenne, 1995b: Interannual and interdecadal variability in United States surface air temperatures, 1910–1987. *Clim. Change* **31**, 35–66.

Dickey, J., M. Ghil, and S. Marcus, 1991: Extratropical aspects of the 40–50-day oscillation in length-of-day and atmospheric angular momentum. *J. Geophys. Res.*, **96**, 2643–2658.

Eliassen, E., B. Machenhauer, and E. Rassmusen, 1970: On a numerical method for integration of the hydrodynamical equations with spectral representation of the horizontal fields, *Rept. 2, Institute for Theoretical Meteorology*, University of Copenhagen, 35pp.

Eubanks, T. M., J. A. Steppe, J. O. Dickey and P. S. Callahan, 1985: A spectral analysis of the Earth's rotation budget. *J. Geophys. Res.*, **90**, 5385–5404.

Ghil, M., 1987: Dynamics, statistics and predictability of planetary flow regimes, in *Irreversible Phenomena and Dynamical Systems Analysis in Geosciences*, C. and G. Nicolis (eds.), Reidel, Boston, pp. 241–283.

_____, and S. Childress, 1987: *Topics in Geophysical Fluid Dynamics: Atmospheric Dynamics, Dynamo Theory and Climate Dynamics*, Springer-Verlag, New York, 485 pp.

_____, and K. Mo, 1991a: Intraseasonal oscillations in the global atmosphere. Part I: Northern hemisphere and tropics. *J. Atmos. Sci.*, **48**, 752–779.

_____, and K. Mo, 1991b: Intraseasonal oscillations in the global atmosphere. Part II: Southern hemisphere. *J. Atmos. Sci.*, **48**, 780–790.

_____, and C. Taricco, 1997: Advanced spectral analysis methods. In *Past and Present Variability of the Solar-Terrestrial System: Measurement, Data Analysis and Theoretical Models*, G. C. Castagnoli and A. Provenzale (Eds.), IOS Press, Amsterdam, in press.

_____, and R. Todling, 1996: Tracking atmospheric instabilities with the Kalman filter. Part II: Two-layer results. *Mon. Wea. Rev.* **124**, 2340–2352.

_____, and R. Vautard, 1991: Interdecadal oscillations and the warming trend in global temperature time series. *Nature*, **350**, 324–327.

_____, and P. Yiou, 1996: Spectral methods: What they can and cannot do for climatic time series. In *Decadal Climate Variability Dynamics and Predictability*, Anderson and Willebrand (Eds.), NATO ASI Series, Vol. I 44, pp. 446–482, Springer-Verlag, Berlin.

_____, S. L. Marcus, J. O. Dickey, and C. L. Keppenne, 1991: *AAM the Movie.* NTSC videocassette AVC-91-063-T1M, Caltech/NASA Jet Propulsion Laboratory, Pasadena, California.

Grotjahn, R., 1993: *Global Atmospheric Circulations: Observations and Theories.* Oxford Univ. Press, N.Y., 430 pp.

Haltiner, G.J., and R.T. Williams, 1980: *Numerical Prediction and Dynamic Meteorology.* John Wiley & Sons, 477 pp.

Held, I. M., 1983: Stationary and quasi-stationary eddies in the extratropical troposphere: theory. In *Large-Scale Dynamical Process in the Atmosphere*, B. J. Hoskins and R. P. Pearce, eds., pp. 127–168, Academic Press, London.

Hide, R., and J.O. Dickey, 1991: Earth's variable rotation. *Science*, **253**, 629–637.

_____, and P.J. Mason, 1975: Sloping convection in a rotating fluid. *Adv. Physics*, **24**, 47–100.

Hurrell, J. W., 1995: Transient eddy forcing of the rotational flow during northern winter. *J. Atmos. Sci.*, **52**, 2286–2301.

Itoh, H., and M. Kimoto, 1998: Weather regimes, low-frequency oscillations, and principal patterns of variability: A perspective of extratropical low-frequency variability. *J. Atmos. Sci.*, sub judice.

Jiang, N., J. D. Neelin, and M. Ghil, 1995: Quasi-quadrennial and quasi-biennial variability in the equatorial Pacific. *Clim. Dyn.* **12**, 101–112.

Jin, F-f., and M. Ghil, 1990: Intraseasonal oscillations in the extratropics: Hopf bifurcation and topographic instabilities. *J. Atmos. Sci.*, **47**, 823–839.

Kalnay, E., et al., 1996: The NCEP/NCAR 40-year reanalysis project. *Bull. Am. Met. Soc.*, **77**, 437-471.

Keppenne, C.L., 1989: *Bifurcations, Strange Attractors, and Low-Frequency Atmospheric Dynamics*, Ph.D. Dissertation, Catholic University of Louvain, 159pp. [Available from Michael Ghil, UCLA Dept. of Atmospheric Sciences, 405 Hilgard Ave., Los Angeles, CA 90095-1565].

_____, 1992: Orographically-forced oscillations in a dynamical model of the Martian atmosphere. *Icarus*, **100**, 598–607.

_____, and M. Ghil, 1993: Adaptive filtering and prediction of noisy multi-variate signals: An application to subannual variability in atmospheric angular momentum. *Intl. J. Bifurcations & Chaos*, **3**, 625–634.

_____, and A.P. Ingersoll, 1995: High-frequency orographically forced variability in a single-layer model of the Martian atmosphere. *J. Atmos. Sci.*, **52** 738–753.

Kimoto, M., 1987: *Analysis of Recurrent Flow Patterns in the Northern Hemisphere Winter*. M.S. thesis, Dept. Atmos. Sci., University of California, Los Angeles, 104 pp. [Available from Michael Ghil, UCLA Dept. of Atmospheric Sciences, 405 Hilgard Ave., Los Angeles, CA 90095-1565].

———, and M. Ghil, 1993a: Multiple flow regimes in the Northern Hemisphere winter. Part I: Methodology and hemispheric regimes. *J. Atmos. Sci.*, **50**, 2625–2643.

———, and M. Ghil, 1993b: Multiple flow regimes in the northern hemisphere winter. Part II: Sectorial regimes and preferred transitions. *J. Atmos. Sci.*, **50**, 2645–2673.

———, ———, and K. Mo, 1991: Spatial structure of the 40-day oscillation in the Northern Hemisphere extratropics. In *Proc. VIIIth Conf. Atmos. & Oceanic Waves & Stability*, American Meteorological Society, Boston, 115–116.

Knutson, T.R., and K.M. Weickmann, 1987: 30–60 day atmospheric oscillations — composite life-cycles of convection and circulation anomalies. *Mon. Wea. Rev.*, **115**, 1407–1436.

Kurihara, A., 1965: On the use of implicit and iterative methods for the time integration of the wave equation. *Mon. Wea. Rev.*, **93**, 33–46.

Kushnir, Y, 1987: Retrograding wintertime low-frequency disturbances over the north Pacific Ocean, *J. Atmos. Sci.*, **44**, 2727–2742.

Lau, K.-M., and Chan, P., 1985: Aspects of the 40–50 day oscillation during the northern hemisphere winter as inferred from outgoing longwave radiation, *Mon. Wea. Rev.*, **11**, 1889–1909.

———, and L. Peng, 1987: Origin of low-frequency (intraseasonal) oscillations in the tropical atmosphere. Part I: Basic theory. *J. Atmos. Sci.*, **44**, 950-972.

Lau, N.-C., 1988: Variability of the observed midlatitude storm tracks in relation to low-frequency changes in the circulation pattern. *J. Atmos. Sci.*, **45**, 2718–2743.

_____, and M.J. Nath, 1987: Frequency-dependence of the structure and temporal development of wintertime tropospheric fluctuations — comparison of a GCM with observations. *Mon. Wea. Rev.*, **115**, 251–271.

Legras, B., and M. Ghil, 1985: Persistent anomalies, blocking and variations in atmospheric predictability. *J. Atmos. Sci.*, **43**, 433–471.

Lorenz, E.N., 1963: The mechanics of vacillation. *J. Atmos. Sci.*, **20**, 448–464.

Madden, R. A., 1988: Large intraseasonal variations in wind stress over the tropical Pacific. *J. Geophys. Res.*, **93**, 5333–5340.

_____, and Julian, P., 1971: Detection of a 40–50 day oscillation in the zonal wind in the tropical Pacific. *J. Atmos. Sci.*, **28**, 702–708.

_____, and _____, 1972: Description of global-scale circulation cells in the tropics with a 40–50 day period, *J. Atmos. Sci.*, **29**, 1109–1123.

Magaña, V., 1993: The 40- and 50-day oscillations in atmospheric angular momentum at various latitudes. *J. Geophys. Res.*, **98**, 10441–10450.

Mann, M. E., and J. Lees, 1996: Multitaper spectral analysis for climate applications: Testing for signals against a robustly estimated red-noise background. *Clim. Change*, **33**, 409–445.

Marcus, S., 1990: *Intraseasonal Oscillations in the Earth-Atmosphere System*, Ph.D. Thesis, 184pp., University of California at Los Angeles. [Available from Steven Marcus, Jet Propulsion Laboratory, California Institute of Technology, 4800 Oak Park Dr., Pasadena, CA 91109.]

_____, M. Ghil, and J.O. Dickey, 1994: The extratropical 40-day oscillation in the UCLA general circulation model. Part I: Atmospheric angular momentum, *J. Atmos. Sci.*, **51**, 1431–1446.

_____, _____, and _____, 1996: The extratropical 40-day oscillation in the UCLA general circulation model. Part II: Spatial structure. *J. Atmos. Sci..*, **53**, 1993–2014.

McAvaney, B. J., W. Bourke, and K. Puri, 1978: A global spectral model for simulation of the general circulation. *J. Atmos. Sci.*, **35**, 1557–1583.

Mo, K. C., and M. Ghil, 1987: Statistics and dynamics of persistent anomalies. *J. Atmos. Sci.*, **44**, 877–901.

Namias, J., 1950: The index cycle and its role in the general circulation. *J. Meteor.*, **7**, 130–139.

Oort, A, 1983: Global Atmospheric Circulation Statistics, 1958–1973, *NOAA Professional Paper 14,,* U.S. Department of Commerce, Rockville, Md., 180pp.

Orszag, S., 1970: Transform method for the calculation of vector-coupled sums: Application to the spectral form of the vorticity equation. *J. Atmos. Sci.*, **27**, 890–895.

Pedlosky, J., 1987: *Geophysical Fluid Dynamics*. Springer-Verlag, New York, 710 pp.

Penland, C., M. Ghil, and K. M. Weickmann, 1991: Adaptive filtering and maximum entropy spectra with application to changes in atmospheric angular momentum. *J. Geophys. Res.*, **96**, 22659–22671.

Percival, D. B., and A. T. Walden, 1993: *Spectral Analysis for Physical Applications — Multitaper and Conventional Univariate Techniques*. Cambridge University Press, 580 pp.

Plaut, G., and R. Vautard, 1994: Spells of low frequency oscillations and weather regimes in the Northern Hemisphere. *J. Atmos. Sci.*, **51**, 210–236.

Preisendorfer, R. W., 1988: *Principal Component Analysis in Meteorology and Oceanography*. C. D. Mobley, Ed., Elsevier Science Publishing Co., Inc., N. Y., 425 pp.

Press, W. B., B. P. Flannery, S. A. Teukolski, and W. T. Vetterling, 1992: *Numerical Recipes in FORTRAN, Second Edition*, Cambridge University Press, 963 pp.

Rabiner, L.R., and B. Gold, 1975: *Theory and Application of Digital Signal Processing.* Prentice-Hall, Englewood Cliffs, N.J., 342 pp.

Rossby, C.-G., and collaborators, 1939: Relation between variations in the intensity of the zonal circulation of the atmosphere and the displacements of the semi-permanent centers of action. *J. Marine Res.*, **2**, 38–55.

Slepian, D., 1978: Prolate spheroidal wave functions, Fourier analysis and uncertainty - V: The discrete case. *Bell Syst. Tech. J.*, **57**, 1371–1429.

Slingo, J. N., et al., 1996: Intraseasonal oscillations in 15 atmospheric general circulation models - results from an AMIP diagnostic subproject. *Clim. Dyn.*, **12**, 325-357.

Smagorinsky, J., 1953: The dynamical influence of large-scale heat sources and sinks on the quasi-stationary mean motions of the atmosphere. *Quart. J. Roy. Meteor. Soc.* **79**, 342–66.

Strong, C.M., F-f. Jin, and M. Ghil, 1993: Intraseasonal variability in a barotropic model with seasonal forcing. *J. Atmos. Sci.*, **50**, 2965–2986.

_____, _____, and _____, 1995: Intraseasonal oscillations in a barotropic model with annual cycle, and their predictability. *J. Atmos. Sci.*, **52**, 2627–2642.

Thomson, D.J., 1982: Spectrum estimation and harmonic analysis. *Proc. IEEE*, **70**, 1055–1096.

Tribbia, J., and M. Ghil, 1990: Forced zonal flow over topography and the 30–60 day oscillation in atmospheric angular momentum, NCAR 0501/89-5, National Center for Atmospheric Research, Boulder, CO, 26 pp.

Van Loon, H, and J.C. Rogers, 1978: The seesaw in winter temperatures between Greenland and northern Europe. Part I: General description. *Mon. Wea. Rev.*, **106**, 296–310.

Vautard, R., and M. Ghil, 1989: Singular spectrum analysis in nonlinear dynamics, with applications to paleoclimatic time series, *Physica D*, **35**, 395–424.

_____, K. Mo, and M. Ghil, 1990: Statistical significance test for transition matrices of atmospheric Markov chains. *J. Atmos. Sci.*, **47**, 1926–1931.

_____, P. Yiou, and M. Ghil, 1992: Singular spectrum analysis: a toolkit for short, noisy chaotic time series. *Physica D*, **38**, 95–126.

Wallace, J.M., 1983: The climatological mean stationary waves: Observational evidence. In *Large-Scale Dynamical Processes in the Atmosphere*, B.J. Hoskins and R.P. Pearce (eds.), Academic Press, pp. 27–53.

_____, and M.L. Blackmon, 1983: Observations of low-frequency atmospheric variability. In *Large-Scale Dynamical Processes in the Atmosphere*, B.J. Hoskins and R.P. Pearce (eds.), Academic Press, pp. 55–94.

_____, and D. S. Gutzler, 1981: Teleconnections in the geopotential height field during the Northern Hemisphere winter. *Mon. Wea. Rev.* , **109**, 784-812.

Weickmann, K.M., G. Lussky, and J. Kutzbach, 1985: Intraseasonal (30–60 day) fluctuations of outgoing longwave radiation and 250 mb streamfunction during northern winter, *Mon. Wea. Rev.*, **113**, 941–961.

Weimer, W., and H. Haken, 1989: Chaotic behavior and subcritical formation of flow patterns of baroclinic waves for finite dissipation. *J. Atmos. Sci.*, **46**, 1207–1218.

Yasunari, T., 1981: Structure of an Indian Summer monsoon system with around 40-day period. *J. Met. Soc. Japan*, **59**, 226–354.

Yiou, P., M. Ghil, J. Jouzel, D. Paillard, and R. Vautard, 1994: Nonlinear variability of the climatic system, from singular and power spectra of late Quaternary records. *Clim. Dyn.*, 9, 371–389.

_____, E. Baart, and M. F. Loutre, 1996: Spectral analysis of climate data. *Surveys Geophys.*, **17**, 619–663.

Figure captions

Fig. 1. Time-average zonal mean of (a) the zonal wind component (in ms^{-1}) and (b) geopotential height (in m) for the 100-year December-January-February (DJF) simulation of the model. In (a) and (b), the solid and dashed lines denote the upper- and lower-layer values, respectively; the heights in (b) are deviations from the global average ϕ_i of either layer.

Fig. 2. Northern Hemisphere (NH) climatology for the 100-year DJF model simulation. (a) Streamfunction, averaged over the model's two layers; negative values indicated by dashed lines, while the contour interval is $1*10^7 \, m^2 s^{-1}$. (b) As in (a) but for the upper-layer zonal wind; the contour interval is 5 ms^{-1}.

Fig. 3. Variability of the upper-layer streamfunction. (a) Low-frequency standard deviation (based on 5-day mean fields); (b) high-frequency standard deviation (based on deviations from the 5-day means). Contour interval in both (a) and (b) is $1*10^6 \, m^2 s^{-1}$.

Fig. 4. MEM power spectra of atmospheric angular momentum (AAM) by latitude belt in: (a) the model and (b) the observations. The power at each latitude has been multiplied by the frequency. The units are m^2s^{-3} and the contour interval is 0.015, with values higher than 0.075 shaded. The vertical scale represents latitude. The bottom horizontal scale shows the decimal logarithm of the frequency expressed in cycles/(3 days), and the top one the period in days. The heavy open circles represent MTM peaks which passed a Fisher test with a significance threshold of 99.5%.

Fig. 5. SSA eigenvalue spectra of (a) model and (b) observed NH AAM time series. The window size used is $M = 40$ ($M\Delta$=120 days); the SSA eigenvalues are sorted in decreasing order and represented on a logarithmic scale; the abscissa denotes eigenvalue index. Error bars calculated using the heuristic variance formula of Ghil and Mo (1991a).

Fig. 6. Filtered AAM time series for (a) model and (b) observed NH AAM. The filtered time series were produced by retaining only the intraseasonal modes from each SSA-filtered time series (see text for details). The abscissa denotes time in years, with tick marks corresponding to January 1, and the ordinate NH AAM, centered and normalized by its standard deviation.

Fig. 7. Composites of the model's upper-layer streamfunction-anomaly fields showing the (a) high, (b) decreasing, (c) low, and (d) increasing phase of the 40-day oscillation. The composites are keyed to the model's NH AAM time series that isolates the 40-day variability. The contour interval is $1*10^6$ m^2s^{-1}.

Fig. 8. Composites of the observed 200-mb streamfunction-anomaly fields showing the (a) high, (b) decreasing, (c) low, and (d) increasing phase of the 40-day oscillation. The composites are keyed to the observed NH AAM time series that isolates only the 40-day variability. The contour interval is $1*10^6$ m^{2}s^{-1}.

Fig. 9 Same as Fig. 7 for the 70-day oscillation over the model's Euro-Atlantic sector only (30° to 90°N, 80°W to 40°E). The composites are keyed to the model's NH AAM time series that isolates the 70-day variability. The contour interval is $1*10^6$ m^{2}s^{-1}.

Fig. 10. Same as Fig. 8, for the 70-day oscillation. The composites are keyed to the observed NH AAM time series that isolates the 70-day variability. The contour interval is $1*10^6$ m^{2}s^{-1}.
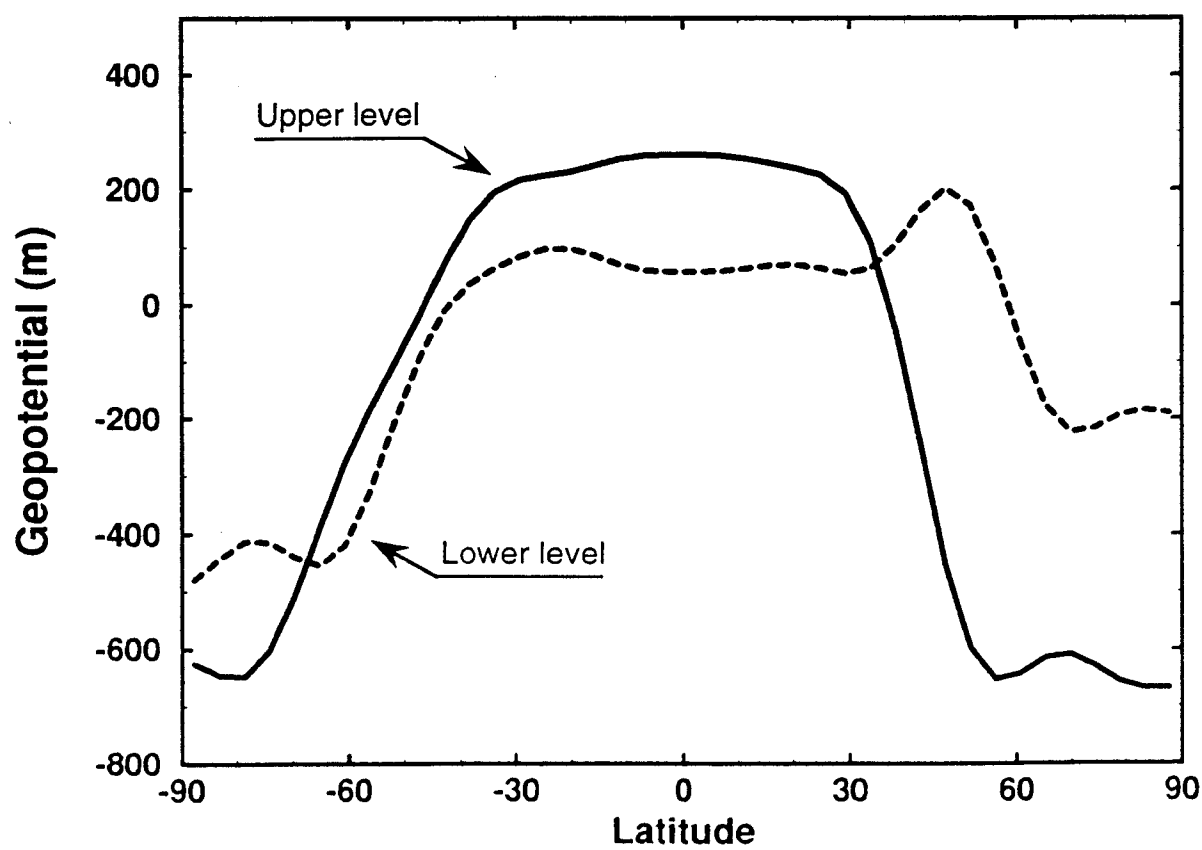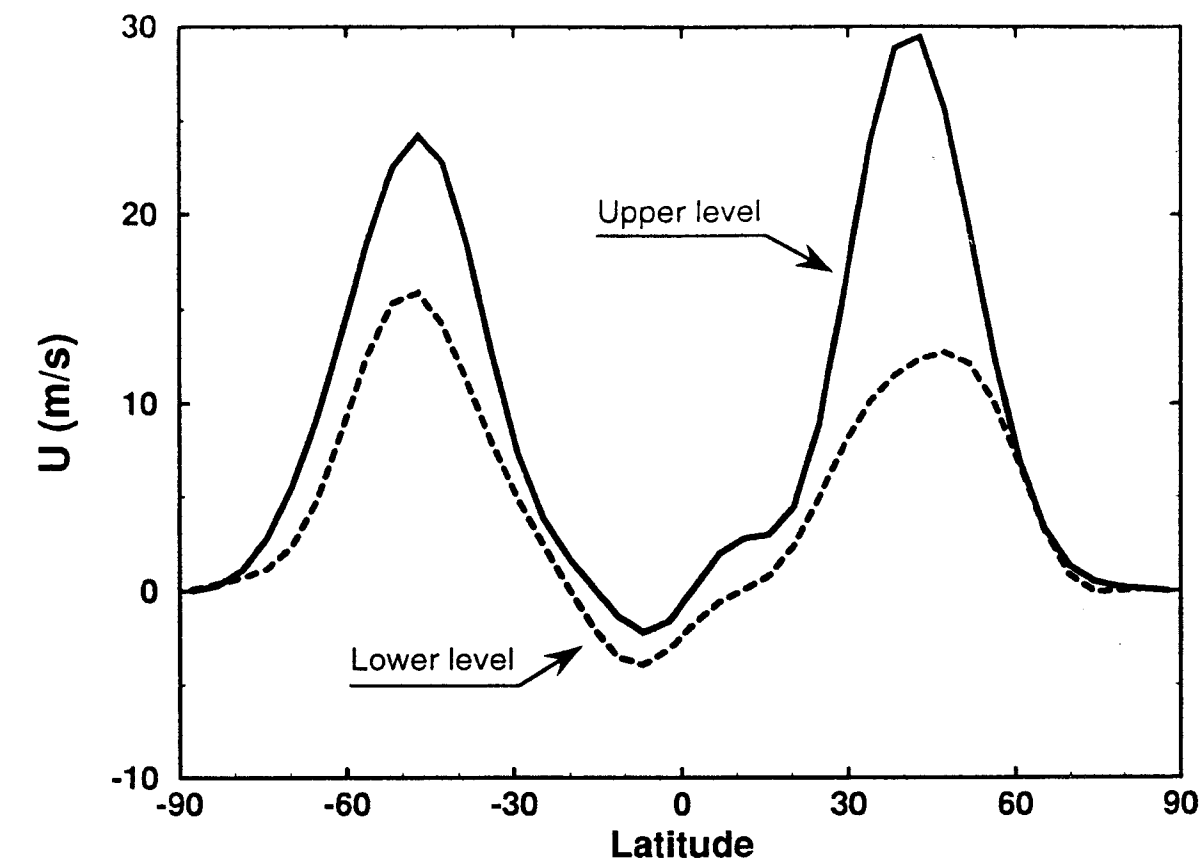
Fig. 1

a) Streamfunction
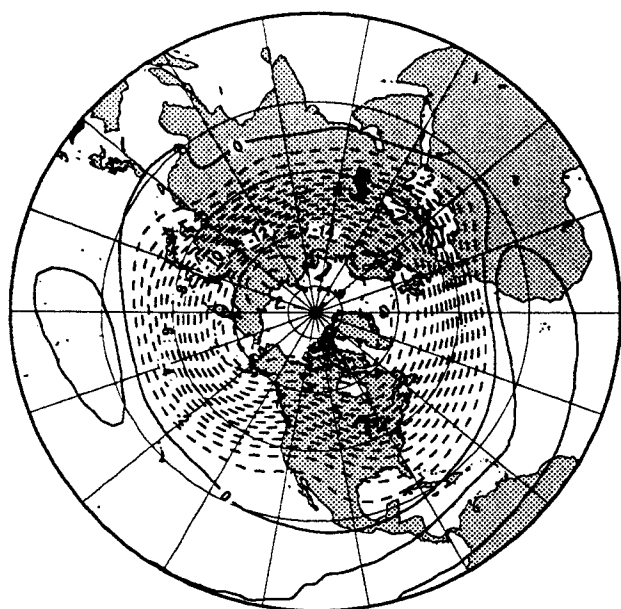
b) Zonal wind
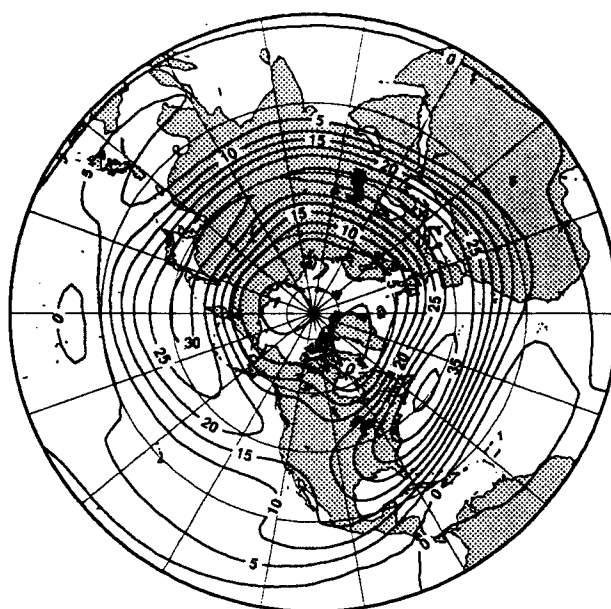
Fig. 2

a) Low frequency

b) High frequency

Fig. 3

a) Model

Period (days)

b) Observations

Period (days)

Fig. 4

a) Model

b) Observations

Fig. 5

a) Model

b) Observations
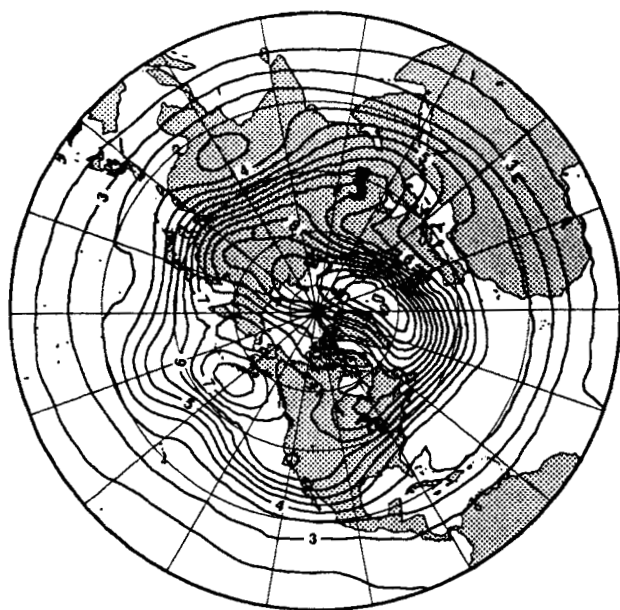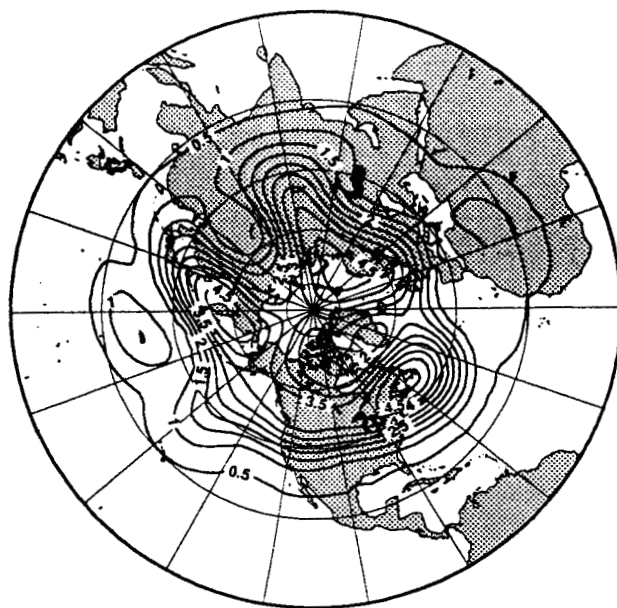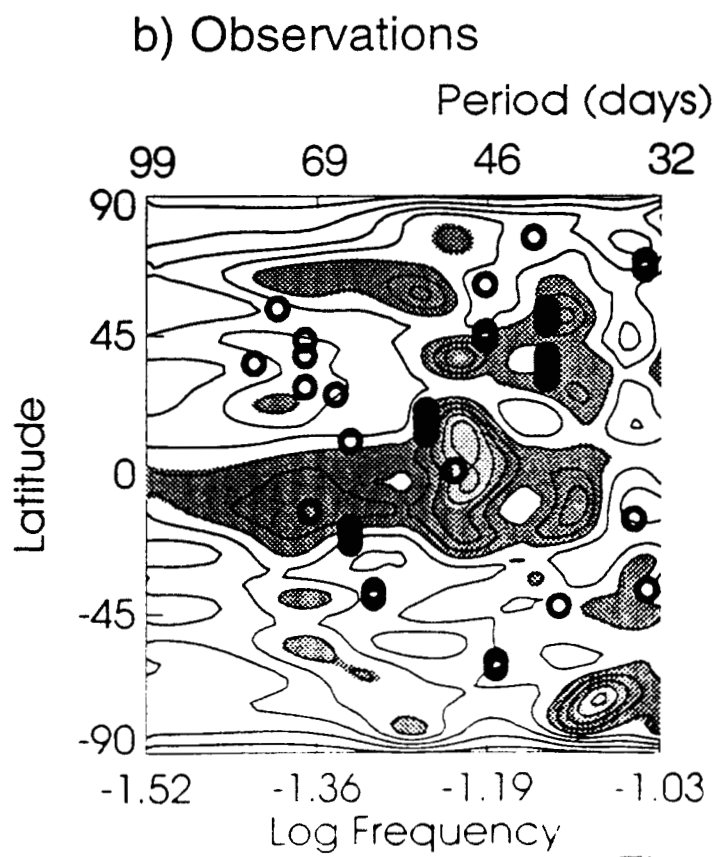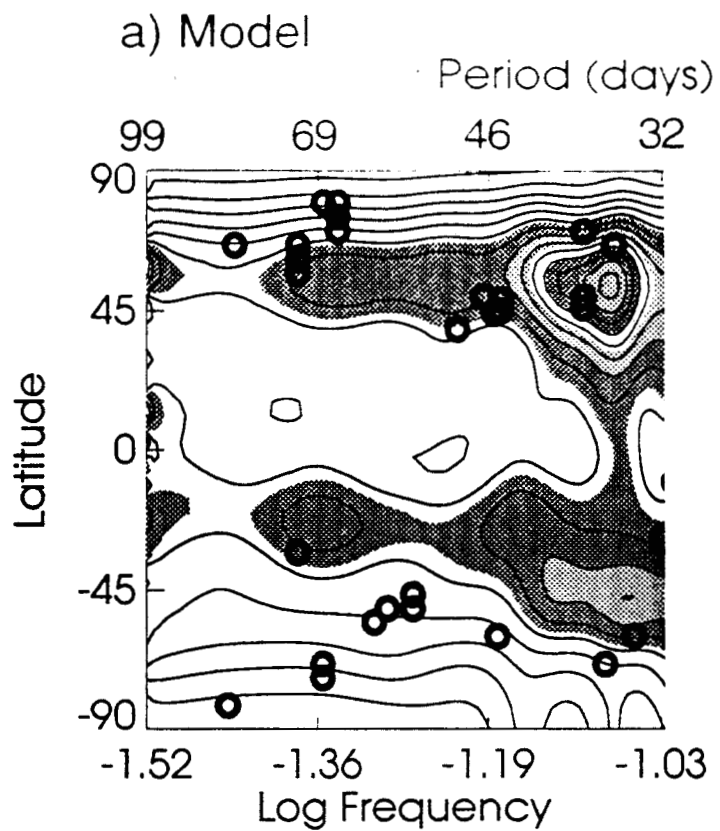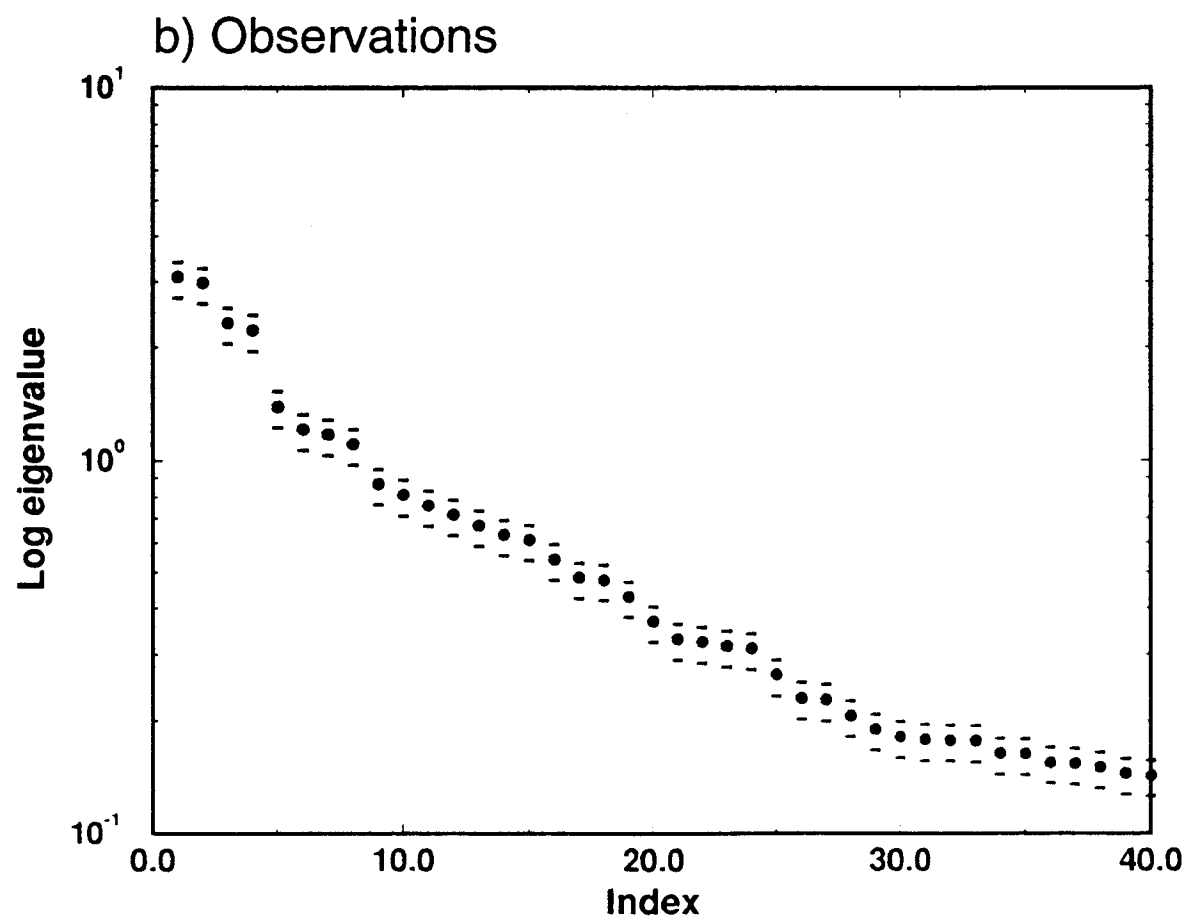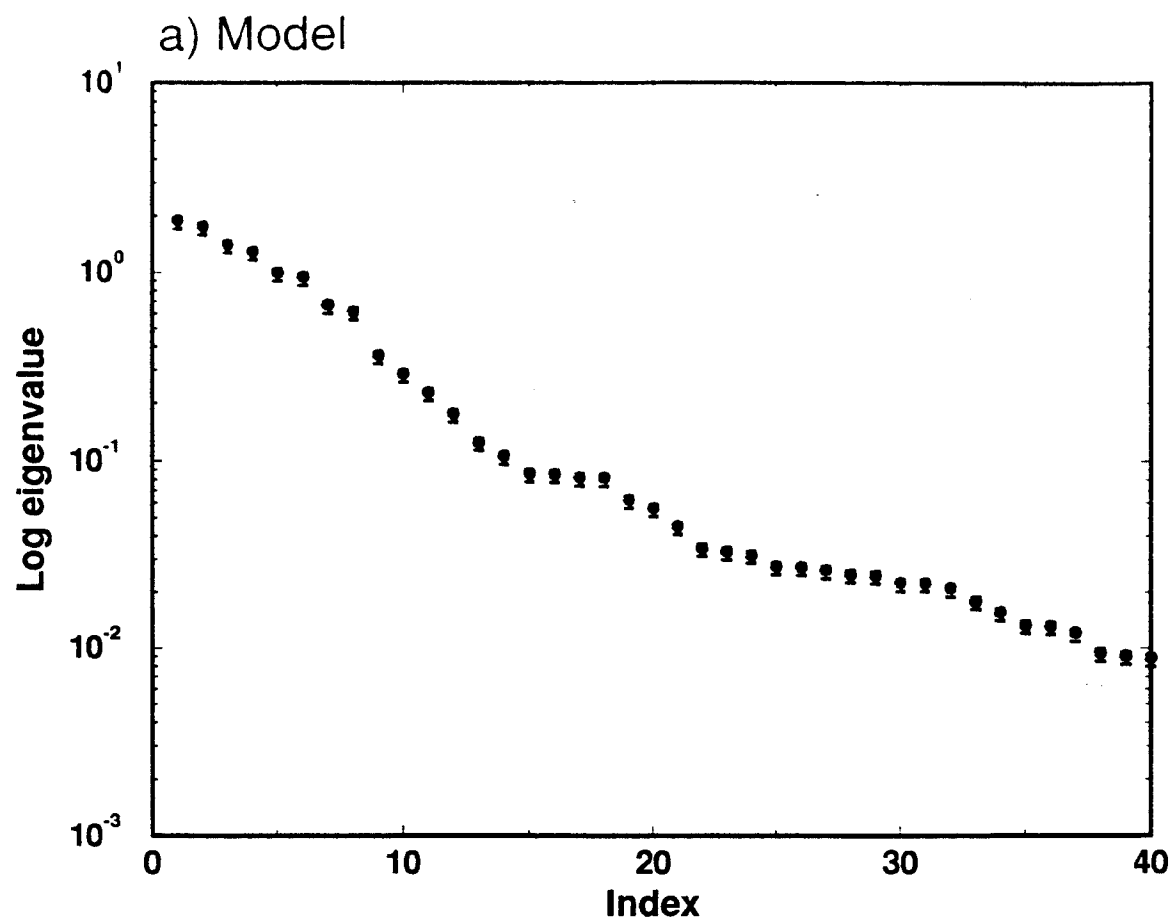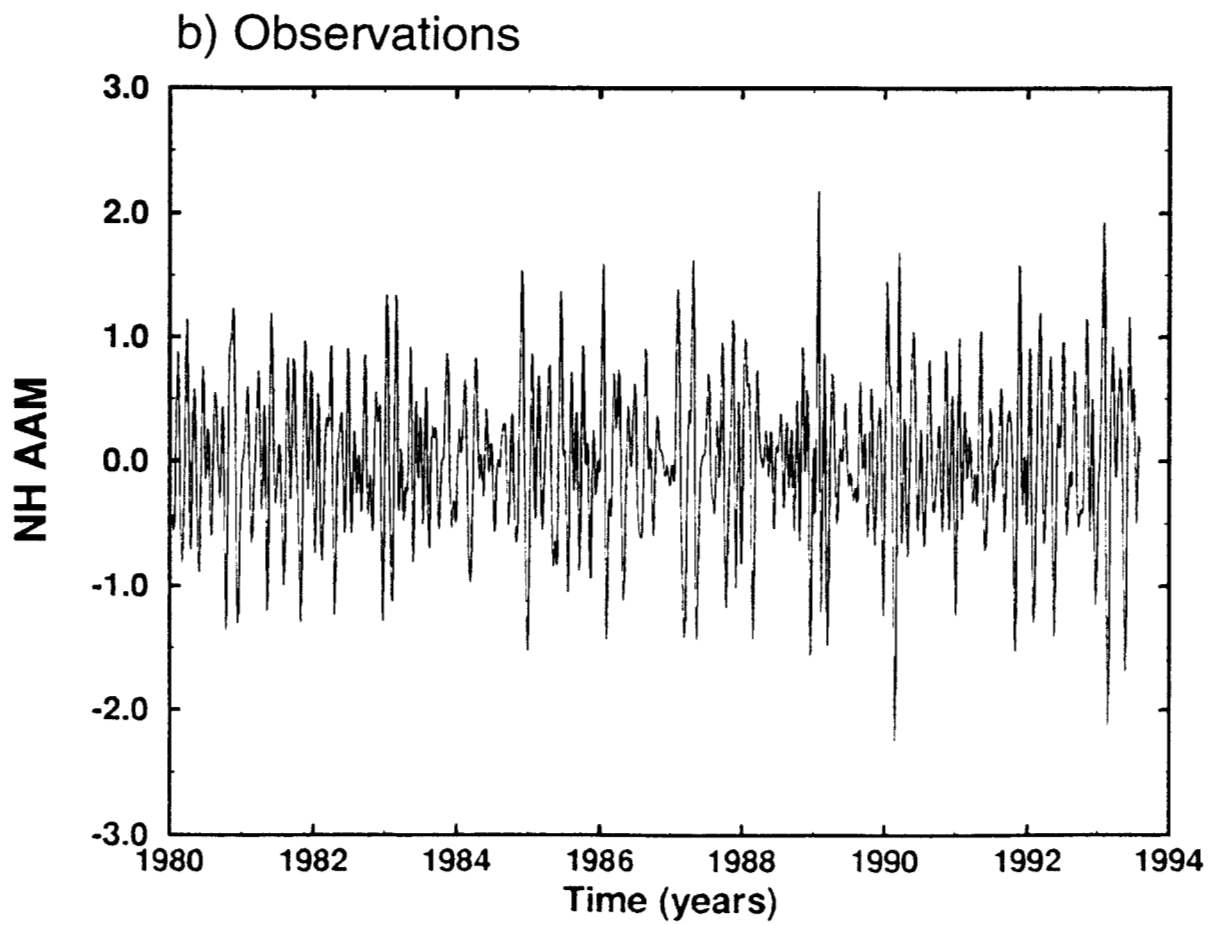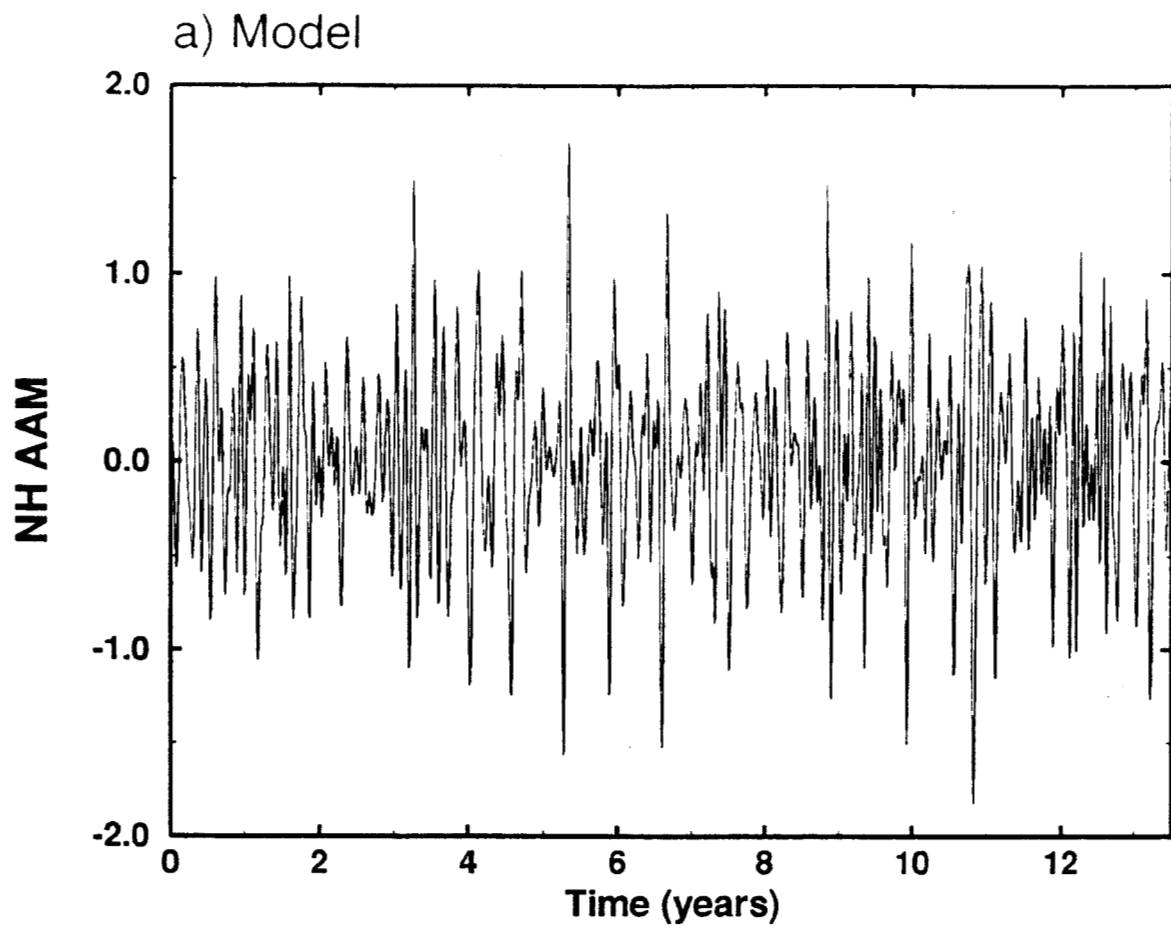
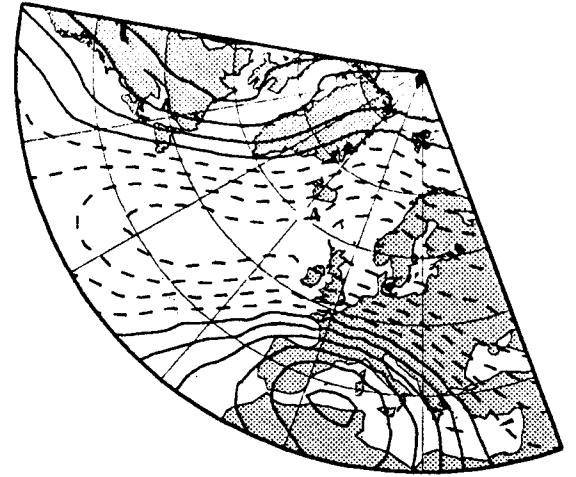Fig. 6
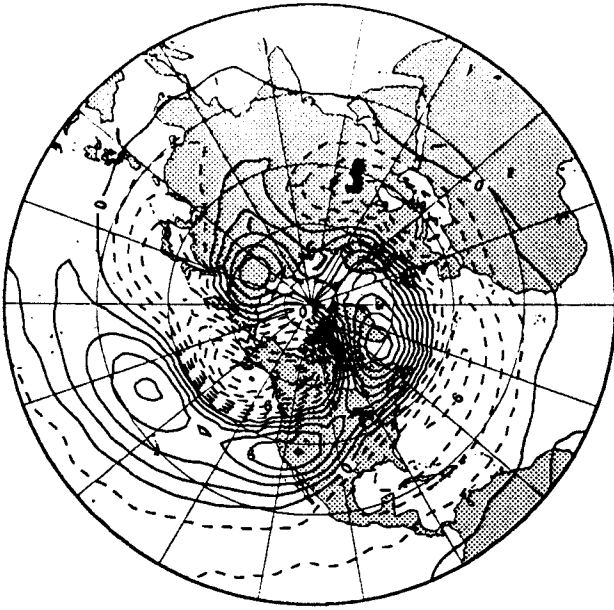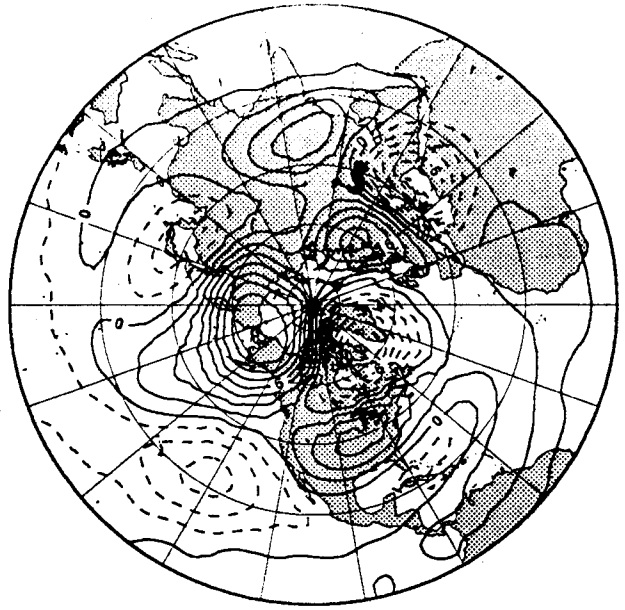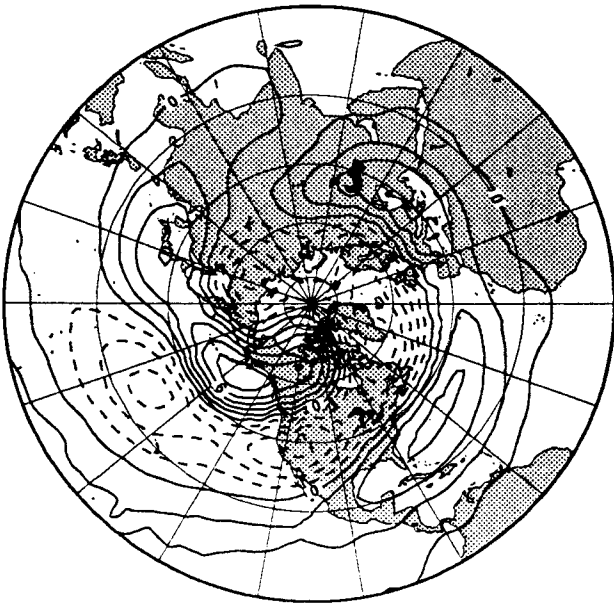
a) High
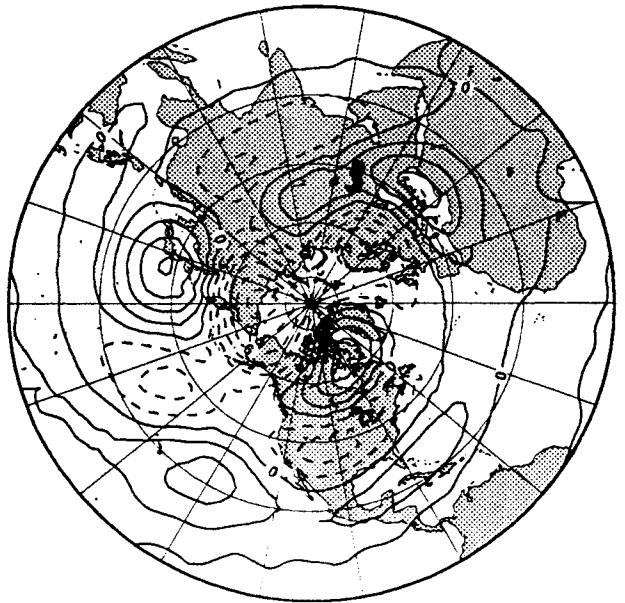
b) Decr
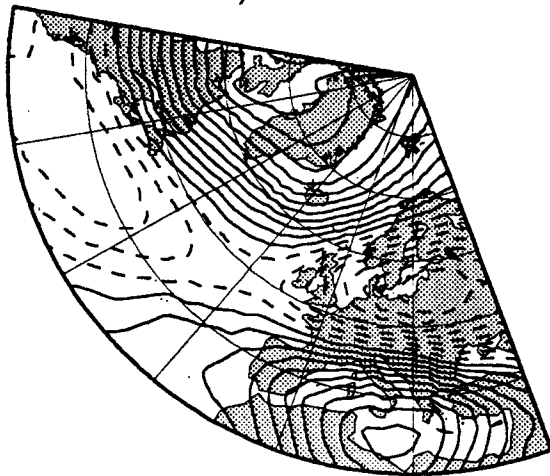
c) Low

d) Incr

Fig. 7
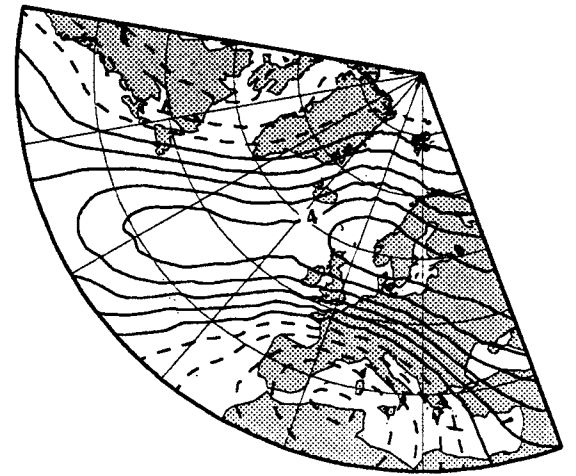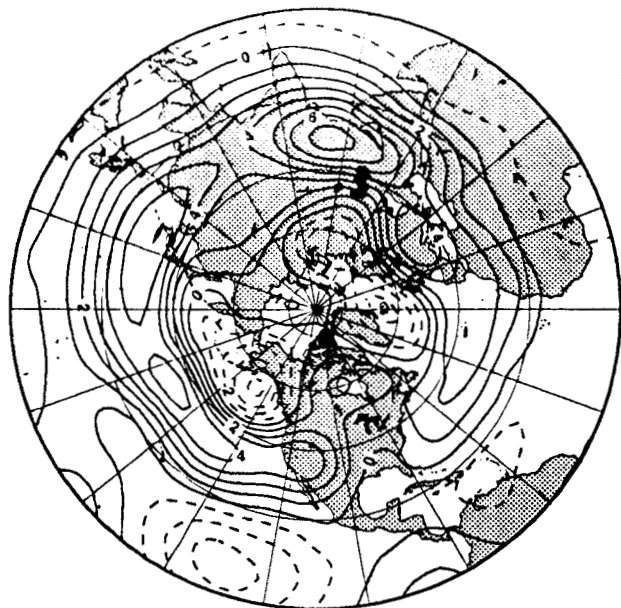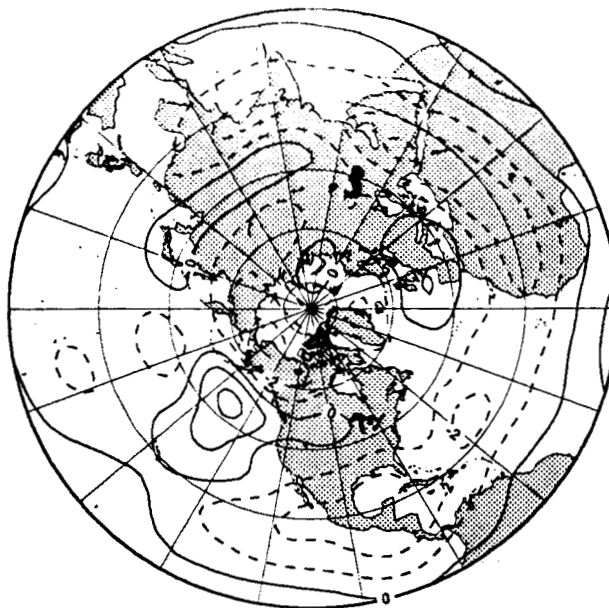
a) High
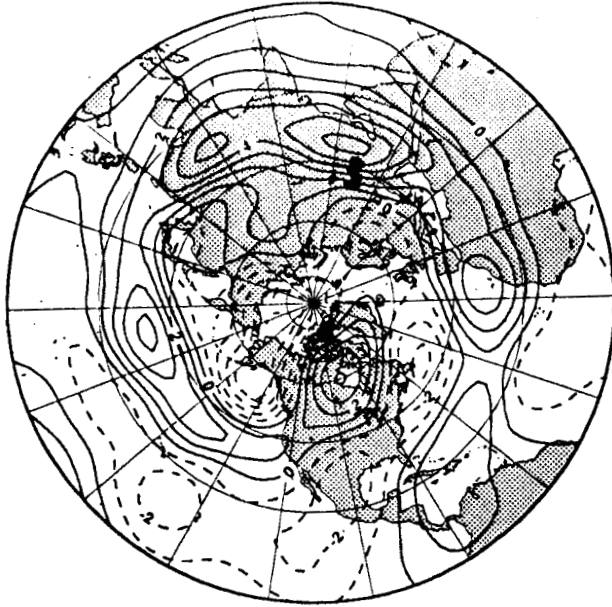
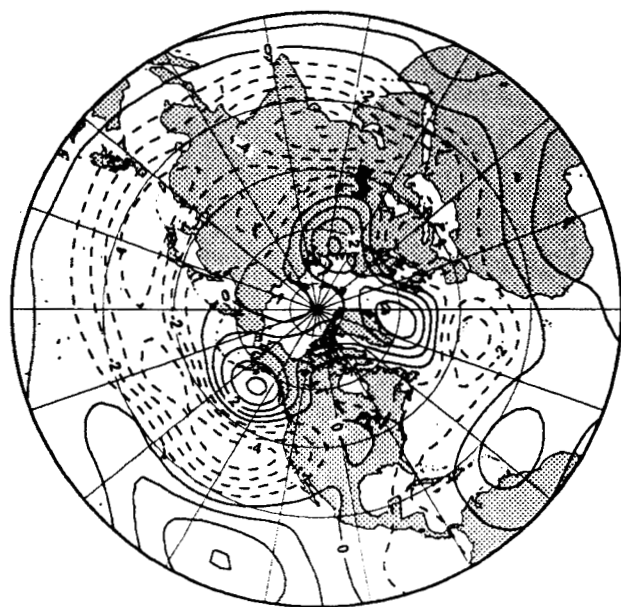b) Decr
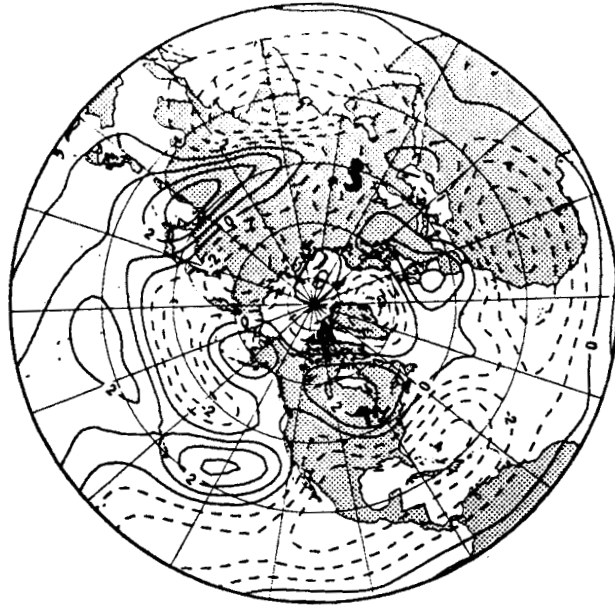
c) Low
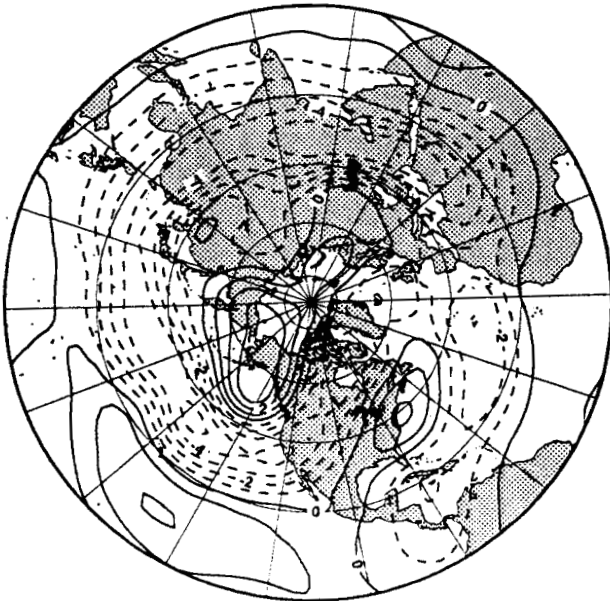
d) Incr
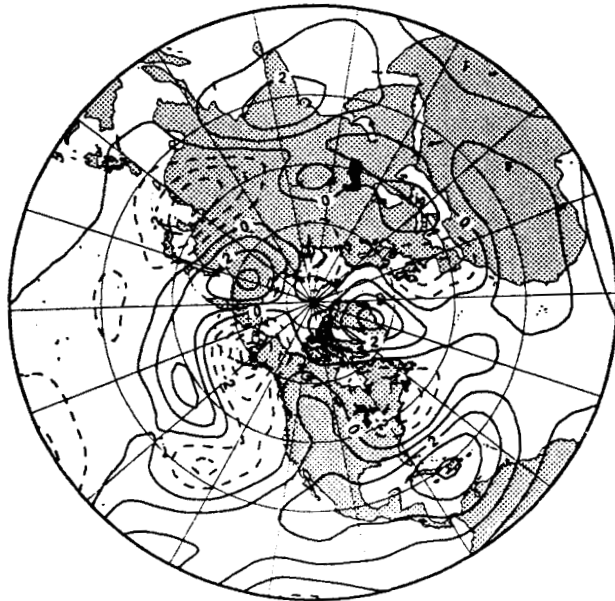
Fig. 8

a) High
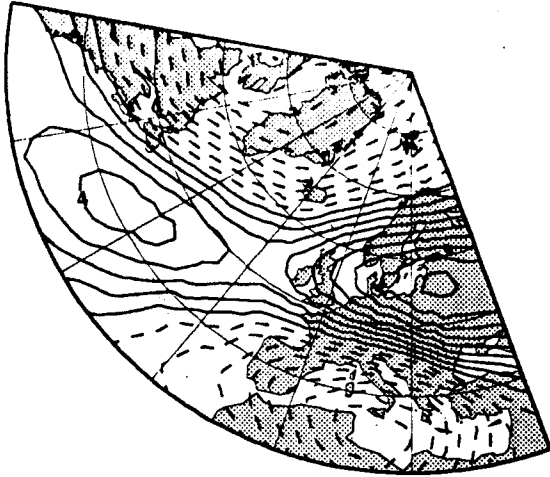
b) Decr

c) Low

d) Incr

Fig. 9

a) High

b) Decr

c) Low

d) Incr

Fig. 10